Texas A&M University
J. Mike Walker'66 Department of Mechanical Engineering
Turbomachinery Laboratory
Tribology Group

EXPERIMENTAL FORCE COEFFICIENTS IN A SEALED ENDS SFD SUPPLIED WITH LUBRICANT THROUGH A CHECK VALVE

Annual Progress Report to the TAMU Turbomachinery Research Consortium

TRC-SFD-02-20

by

Luis San Andrés
Mast-Childs Chair Professor
Principal Investigator

Bryan Rodríguez
Graduate Research Assistant

June 2020

EXECUTIVE SUMMARY

EXPERIMENTAL FORCE COEFFICIENTS IN A SEALED ENDS SFD SUPPLIED WITH LUBRICANT THROUGH A CHECK VALVE

LUIS SAN ANDRÉS AND BRYAN RODRÍGUEZ, JUNE 2020

Squeeze film dampers (SFDs) add damping to rotor-bearing systems hence reducing rotor vibrations, aiding to suppress rotor instabilities; and along with a structural elastic support element, isolate the rotor from a stator or casing. End seals like O-rings (ORs), piston rings (PRs) and end plates reduce side leakage and air ingestion while amplifying the viscous damping in configurations with limited physical space. OR end seals are of particular interest as they also add both centering stiffness and damping to a SFD.

Experiments conducted in 2019-20 continue to quantify the dynamic forced response of an ORs sealed SFD (short length span L/D=0.2) presently supplied with a light lubricant (ISO VG2) at a low pressure (0.69 barg). The lubricant flows into the film land through a mechanical check valve (preventing back flow) and exits through a hole midway between the damper center plane and an OR. A large plenum upstream of the check valve fills in with lubricant and serves to attenuate pressure fluctuations.

Multiple sets of single-frequency dynamic loads, 10 Hz to 120 Hz, produce circular centered orbits with amplitudes (r) to 15% of the damper clearance (c = 0.279 mm). The experimental results identify the test structure, ORs and SFD force coefficients, namely, stiffness, mass and damping (K, M, C). The ORs force coefficients are frequency independent with a sizeable direct stiffness (K_{OR}), ~ ½ of the rig structural stiffness. The ORs also show a quadrature stiffness K_0; such that (K_0/K_{OR}) ~ 0.26 reveals a significant material loss factor. The OR viscous damping coefficient is also significant and contributes to about 10% of the damping of the lubricated system. The squeeze film lands produce the other 90% damping. The identified SFD force coefficients show a near constant magnitude for three orbit radii (r/c)=0.15c max. The fluid inertia (M_{SFD}), four fold the bearing physical mass, is so large that the system natural frequency drops from ~200 Hz (structure +ORs) to 90 Hz. The experimental force coefficients, C_{SFD} ~ 0.7C* and M_{SFD} ~ 1.1 M^*, moderately agree with predictions for a fully sealed SFD. The discrepancy in viscous damping is due to oil vapor cavitation and air entrainment into the film lands, as evidenced by recorded dynamic pressures in the film. Importantly enough, dynamic peak-to-peak pressures in the plenum upstream of the check valve show pressure fluctuations with magnitude proportional to the whirl frequency. Hence, unsuspectedly, the check valve did allow for lubricant backflow.

Table of Contents

Nomenclature

c	Damper radial clearance [m]
C	Damping coefficient [N-s/m]
C^*	Analytical damping coefficient [N-s/m]
$\underline{C}$	Normalized damping coefficient [-]
C_{st}	Support structure damping coefficient [N-s/m]
C_{st+OR}	Support structure damping coefficient with O-rings installed [N-s/m]
D	Journal diameter [m]
D_{BC}	Bearing cartridge inner diameter
D_J	Journal outer diameter [m]
e_s	Static eccentricity 45° away from X axes [m]
f_n	Test system natural frequency [Hz]
H	$H = (K - \omega^2 M) + i(\omega C)$. Complex dynamic stiffness [N/m] $i = \sqrt{-1}$
h	Film thickness
K	Stiffness coefficient [N/m]
$K_{0,OR}$	OR quadrature stiffness [N/m]
K_{st}	Support structure stiffness coefficient [N/m]
K_{st+OR}	Support structure stiffness with O-rings installed [N/m]
L	Film axial length [m]
M	Added mass coefficients [kg]
M^*	Analytical added mass coefficient [kg]
$\underline{M}$	Normalized added mass coefficient [-]
M_{BC}	Mass of bearing cartridge [kg]
M_{st}	Structure remnant mass coefficient [kg]
P	Fluid film pressure [bar]
P_S	Supply pressure [bar]
r	Orbit radius [m]
Re_S	$(\rho\omega c^2)/\mu$ Squeeze film Reynolds number [-]
S	Standard deviation [-]
T	$2\pi/\omega$. Period of circular whirl motion [-]

$U_{B,}\, U_P,\, U_v$	Bias, precision and variability uncertainty [%]
v_S	$r\omega$. Squeeze film velocity [m/s]
X, Y	Cartesian coordinate system
z	Axial coordinate [m]
θ	Circumferential coordinate [rad]
μ	Lubricant viscosity [mPa-s]
ϕ_{in}	Feedhole orifice diameter [m]
ω	Excitation frequency [rad/s]
ζ_{st}	Support (dry) structure damping ratio [-]
ζ_{st+OR}	Support (dry) structure damping plus O-ring

Vectors and matrices

a	Absolute acceleration [m/s^2]
C	Damping coefficients [N-s/m]
F	Force
H	Complex dynamic stiffness
K	Stiffness coefficients
M	Inertia coefficients
z	BC displacements relative to journal

Subscripts

BC	Bearing cartridge
CCW	Counter clockwise
CW	Clockwise
L	Lubricated
SFD	Squeeze film damper
st	Support structure
st+OR	Structure with ORs installed
est	Estimated
app	Applied

Abbreviations

DAQS	Data acquisition system
ID	Inner diameter
OR	O-ring
OR	Outer diameter
PR	Piston Ring

Introduction

Squeeze film dampers (SFDs) add damping to rotor-bearing systems hence reducing rotor vibrations, aiding to suppress rotor instabilities; and along with a structural elastic support element, isolate the rotor from a stator or casing [1,2]. Figure 1 depicts a schematic view of a sealed ends SFD in series with a ball bearing supported rotor. The ball bearing inner race holds to a journal, and the annular gap between the ball bearing outer race diameter and the bearing cartridge (BC) hosts a lubricant film. A squirrel cage acting as an elastic support or an anti-rotation pin (dowel pin) prevent rotation of the ball bearing outer race. External forces applied on the rotor make the journal and ball bearing precess or whirl to squeeze the lubricant film, and which develops a hydrodynamic pressure field that produces a reaction force characterized by both damping and inertia force coefficients [1].

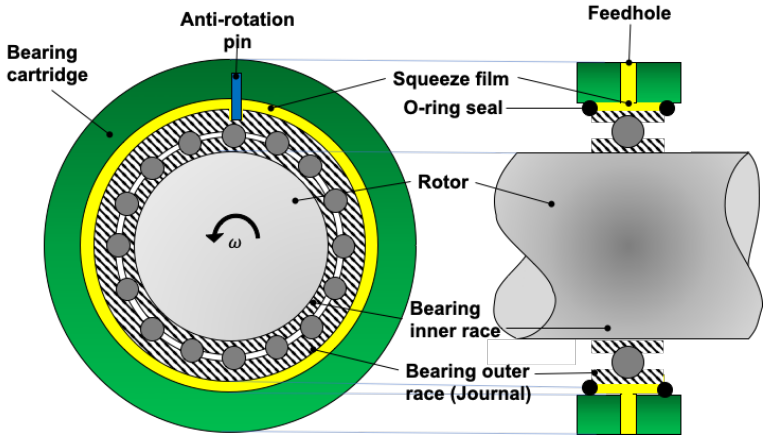

Fig. 1. Schematic views of a one-hole-fed SFD with O-rings sealed ends. Graph modified from original rendition in Ref. [1]

Gas turbines in aircraft engines rely on SFDs in series with ball bearings to safely cross a number of critical speeds and to ensure stable operation at cruise speed or during maneuver conditions. Modern aircraft gas turbines employ short length SFDs (slenderness ratio $L/D \leq 0.2$) to minimize weight and space. Damper dimensions and radial clearance, lubricant physical properties, operating conditions and sealing devices determine the forced performance of SFDs in turbomachinery applications. Sealing devices such as O-rings (ORs) reduce lubricant side leakage, contribute to reduce space and weight, while increasing damping within a limited axial length. Whereas piston rings (PRs) are common sealing elements in SFDs for commercial air breathing engines[3], nitrile ORs are employed in land-based turbomachinery, like compressors and steam turbines [4,5].

Literature Review

Substantial development and application of SFDs emerged in the 1960's, with the widespread use in aircraft gas engines. In 1996, Zeidan et al. [6] present an exhaustive discussion on SFDs advantages and experimental data to the date, and showcase a design procedure for their proper application in turbomachinery. In 2002, Della Pietra and Adiletta [7,8] present a comprehensive review on the research efforts for modeling the SFD forced performance, developing predictive models and experimental validations against test data over forty years. The authors include a complete description on the physical characteristics and operating features of SFDs, including end seal configurations.

The present review discusses published literature on to the experimental parameter identification of force coefficients with a focus on the influence of end seals on the forced performance of SFDs.

Common end seal configurations include O-rings, piston rings and end plate seals to increase damping in SFDs while reducing lubricant supply, air entrainment and entrapment. Elastomeric seals, for example, offer tight sealing, are suitable for configurations with a low static load, and operation near ambient temperature [1]. However, ORs are sensitive to high and low temperatures, and their maximum service temperature is only 120^{o}C [9]. Moreover, this seal type ages quickly and its dynamic forced performance depends on the excitation frequency and amplitude of motion [1]. Conversely, (metal) piston rings (PRs) can withstand a broader temperature range, alas their abutted ends (slits) still allow for substantial lubricant flow [10].

Experimental and analytical efforts in the 1970's advanced toward the understanding on the effects of end seals on the dynamic forced response of SFDs. In 1974, Vance and Kirton [11], experimentally investigate the generation of a fluid hydrodynamic pressure in a long SFD (length over diameter, L/D = 0.96) with a large radial clearance. The authors demonstrate that the OR end seals prevent film pressure variations along the axial direction. In 1978, Feder et al. [12] study a short-length (L/D = 0.3), OR sealed, statically off-centered damper performing circular whirl orbits for its application in aircraft engines. The authors numerically integrate the film pressure profile to determine the force components in the squeeze film and demonstrate increasing magnitude of damping with lubricant supply pressure.

Many of the analytical models produced in this decade render reliable predictions only for damping coefficients, since they are based on classical lubrication theory, assuming that fluid

inertia is negligible. This condition is generally not true for SFDs, due to their larger clearance, operation at high frequencies and use of light viscous lubricants. The squeeze film Reynolds number ranges from 1 to 50, making fluid inertia effects in dampers significant, even lowering considerably the critical speeds of compact turbomachinery. [1].

In the 1980's and 1990's, a wealth of experimental investigations were developed to provide insight, and explanations for some of the measurements and behavior which are not predicted by classical lubrication theory in SFDs [1]. In 1989, Zeidan and Vance [13] conduct flow visualizations in a PRs sealed SFD, given that their operation largely depends on the types of cavitation in the film lands. Film dynamic pressure measurements and direct observations with high speed photography in a clear acrylic housing enable the identification of oil vapor and gaseous cavitation with increasing orbit frequency. Leakage through the PR slits permit air entrance into the film land, thus causing oil gaseous cavitation, while the addition of backup rings provided tight sealing, causing vapor cavitation synchronous with the rotor speed.

In 1990, Zeidan and Vance [14] expand prior work and identify five SFD regimes with distinct types of dynamic fluid cavitation (vapor or gas) and air ingestion and entrapment in the operation of SFDs. The experiments comprise a controlled orbit test rig, at a fixed orbit radius. The test damper features one circumferential freed groove with four inlet holes and serrated PRs sealing the film lands. The authors discern each regime with increasing operating speed and lubricant supply pressure.

In 1996, Kuzdzal and Hustak [15] present the results of a test campaign assessing several SFD configurations, including those that are sealed with three types of O-rings, to show their ability to suppress rotor subsynchronous vibration and attenuate rotor synchronous motions installed in modern compressors. Results from tests with different rotor eccentricities show that an eccentric SFD does not perform well, relative to a centered damper to suppress rotor subsynchronous vibration. The experiments validate their analytical damping equation, demonstrating that damping increases with rotor eccentricity.

In the same year, Zeidan et al. [6] review 25 years of experience researching, experimenting and applying SFDs into high performance turbomachinery. The authors provide design configurations with advantages and practical limitations of SFDs and showcase theoretical models and measurements for parameter identification and prediction of dampers' dynamic forced response. The lecture distinguishes OR supported dampers for their simple design and means of

providing a centering spring within a limited physical envelope. However, predicting ORs' dynamic force characteristics is rather complex due to the material variance and the influence of temperature, frequency and time on its properties. Furthermore, the authors note that OR dampers are incapable of sustaining thrust loads and ORs seats or grooves must be properly offset to center the damper journal within the clearance space.

Also in 1996, Arauz and San Andrés [16] experimentally identify the effect of a circumferential feeding groove on the dynamic forced response of a PR sealed SFD. The sealing elements feature minute axial holes on its outer diameter, introduced by Jung et al. in 1991 [17, 18] to lessen the distorting pressure effect due to the jet-like out flow through the slits of a PR The short-length damper (L/D = 0.2) performs off-centered circular orbits with frequencies ranging from 33 Hz to 83.3 Hz. At excitation frequencies above 67 Hz, lubricant vapor cavitation is present at the damper film lands. The test results show that cavitation reduces damping, while the ability of the sealed damper to generate larger dynamic pressures also increases the occurrence of fluid cavitation at smaller orbit radii.

In the mid 2000's, an aircraft engine manufacturer funded research in SFDs, to investigate various damper operating conditions. Thus, developing an experimental campaign to measure the dynamic forded response of SFDs with operating characteristics similar to those in air breathing engines. Moreover, a predictive model derived from the test data delivers force coefficients over a range of whirl frequencies and orbit amplitudes. The experiments include a variety of damper configurations, namely, addition of feedholes and grooves to short and long film land lengths, with small and large clearances, and two particular end conditions: open to ambient and PR sealed dampers. In 2016, San Andrés et al. [19] summarize the conducted work and major achievements, while giving practitioners definite answers to fundamental questions about SFD operation.

In 2017, Jeung [20] measures film dynamic pressure profiles and identifies force coefficients (damping and added mass) in PR sealed dampers operating with supply pressures below 1 bar and under a range of squeeze film velocities (v_s = 43 mm/s to 86 mm/s). The measurements show flat pressure zones similar to those reported by San Andrés and Díaz in 2002 [21] in an open ends damper, thus, evidencing a regime of oil vapor cavitation and air ingestion, particularly for operation at low an oil supply pressure (0.7 bar). The tests demonstrate that SFD direct damping coefficients do not significantly increase with increasing amplitude of motion, while the SFD added mass coefficients show a large increase with lubricant supply pressure. The dynamic

pressure measurements and video graphic evidence demonstrate that air ingestion and oil cavitation persists in the sealed ends SFD with a low lubricant supply pressure, leading to a decrease in the direct added mass coefficients.

In 2018, San Andrés and Koo [22] further investigate and compare the performance of a SFD sealed with PRs (PR-SFD) and one with ORs (OR-SFD), both lubricated through one feedhole located in the midplane of the film lands. The authors find an increment in the damping coefficient as the oil supply increases from 2.1 bar to 6.2 bar. The added mass coefficients are significant, as they nearly double the magnitude of the test structure mass, but remain constant with increasing supply pressure. At lubricant supply pressures above 2 bar, the OR sealed damper produces 11% more damping, compared to the PR-SFD, since the O-rings seal lubricant better than PRs. Additionally, the OR-SFD produces ~10% more damping by accounting the viscoelastic damping found in the elastomeric seals.

In 2019, San Andrés and Koo [23] identify the dynamic force coefficients of a PR-SFD and a OR-SFD with lubricant flowing through one and three feedholes at the film land midplane. Tests with a lubricant supply pressure of 0.7 bar(g) demonstrate that the OR-SFD produces larger damping coefficients compared to those from the PR-SFD. Additionally, damping increases with statically off-centered circular tests in the OR-SFD by ~35%, while damping remains constant in the PR-SFD. Tests conducted with one feedhole, show a drastic increase in damping and inertia, for both sealed dampers, showing damping and inertia coefficients ~60% and 80% larger, respectively.

In 2020 , San Andrés and Koo [24] present a physical model for a sealed-end damper operating with a bubbly mixture and compare predictions against experimental results. The aim is to quantify the effects of air ingestion in SFDs applied in aircraft engines. In the dynamic load tests, as the whirl frequency $\omega \rightarrow 0$, damping $C \neq 0$, thus evidencing a quadrature stiffness representing the friction of the PR sliding friction.

The aim of this report is to further quantify the forced performance of an OR sealed SFD supplied with a light viscosity lubricant and at low magnitude supply pressure (~0.7 bar(g)). The lubricant is delivered through a mechanical check valve to reduce backflow from the film land. The experimental tests consider a range of orbit sizes and whirl frequencies; however, all conditions maintain the same squeeze film velocity (three total = 3 amplitudes at 3 frequencies).

This report also details the O-rings selection, installation and troubleshooting of the test element, measurements and parameter identification procedures and tests results; namely, damping and inertia force coefficients.

Description of Experimental Facility and Test Damper

Figure 2 depicts the SFD test rig comprising a rigid pedestal, a journal base, four support rods, a test journal, and a bearing cartridge (BC); and Table 1 lists the journal dimensions and measured ISO VG2 lubricant physical properties. The elastic rods support the BC, while the journal is rigidly affixed to a pedestal. The rods provide a structural stiffness (K_{st}) to simulate an elastic squirrel cage.

Two electromagnetic shakers, connected to the BC via stingers, apply single-frequency dynamic loads along axes *X* and *Y*, shown in Figure 2(b), to produce the orbital motion of the BC with amplitude of radius *r*. A hydraulic piston, located 45^o away from the *X* and *Y* axes, pulls a static force to displace the BC to an eccentric position (*e*) with respect to the fixed journal. Installed in the BC, pairs of Eddy current displacement sensors, piezoelectric accelerometers and load cells measure the BC displacements relative to the stationary journal, the BC acceleration components and the applied loads along the *X* and *Y* directions.

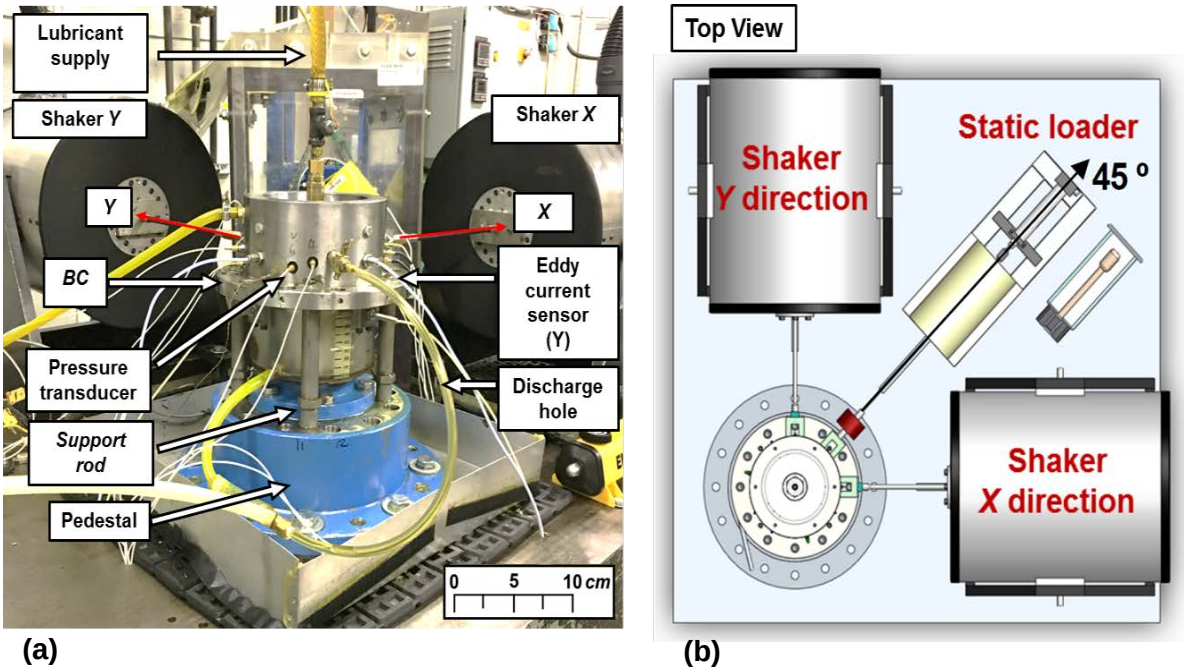

(a) (b)

Fig. 2 (a) Photograph and (b) schematic top view of SFD test rig with electromagnetic shakers and static loader [15].

Table 1. Dimensions of SFD test section and lubricant properties.

Journal diameter, D	126.6± 0.004 mm
Axial film land length, L	25.4± 0.01 mm
Radial clearance, c	0.279 ± 0.006 mm
Feedhole diameter, ϕ_{in}	3.81± 0.01 mm
Location, z=0 and θ_{in}	45^o
Discharge hole diameter, ϕ_{out}	4.50 ± 0.01 mm
Location, z= ¼ L and θ_{out}	240^o
ISO VG 2 oil	
Viscosity @25^{o}C, μ	3.06 ± 0.01 mPa-s
Density @25^{o}C, ρ	780 ± 0.02 kg/m^3
O-rings [4]	**Buna-N AS568 #244**
Outer diameter	114.56 ± 0.10 mm
Inner diameter	107.54 ± 0.76 mm
Ring thickness	3.53 ± 0.10 mm

The short length SFD has a film axial length L = 25.4 mm, with diameter D = 127 mm, and radial clearance c = 0.279 mm ± 0.006 mm. Appendix A details the procedure to measure measured radial clearance. Figures 3 and 4 show schematic views of the journal and BC that showcase the flow of lubricant through the center of the stationary journal into a plenum (dead volume) and then through a check valve at θ_{in}= 45^o to exit into the middle plane of the film land length. The ORs installed in grooves at the edges of the film land, top and bottom, perfectly seal the small film volume in the squeeze film land. Oil exists the damper through an orifice with diameter ϕ_{out} = 4.5 mm located at θ_{out} =240^o and at z = ¼ L, above the middle plane of the film land length.

Figure 4 shows (a) a photograph of the test journal, and schematic views of (b) a cross section of the journal with dimensions, and (c) an inset showcasing the O-rings (OR) locations, and the lubricant feedhole and lubricant discharge hole. The test journal has two parts: a journal bottom base and a top sleeve that connects to the oil inlet supply line through a large *dead* volume equaling 52.6 cm^3. The journal, made of two parts, allows to insert from the inside a mechanical check valve prior to its assembly and affixing to the rigid support base, see Fig. 3(b). The check valve with diameter ϕ_{in} = 3.81 mm prevents lubricant backflow into the dead volume. Note that a piezoelectric pressure transducer records the pressure in the said internal plenum or dead volume. Prior to tests

with a lubricated system, the test journal plenum is filled with oil, before installing the pressure sensor in the journal sleeve.

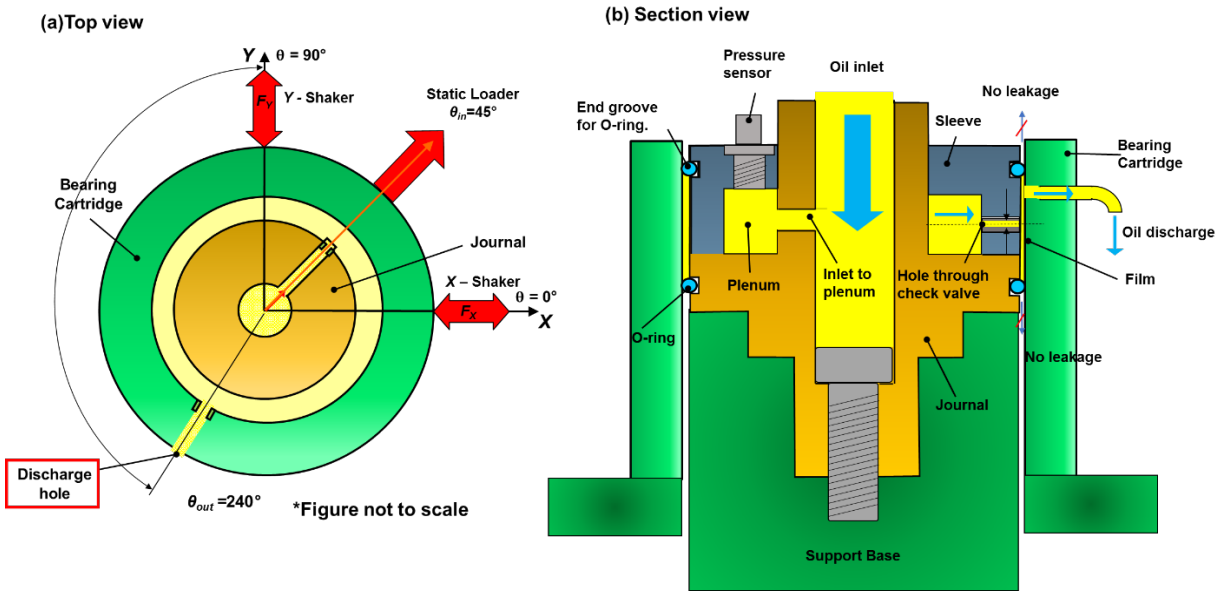

Fig. 3 Schematic views (a) from top to feature one lubricant feedhole (θ_{in} = 45º, z = 0) and a discharge hole (θ_{out} = 240º, z = +¼ L) location, (b) cross-section of journal and BC showing ORs installed. (Drawings not to scale and with exaggerated features)**.**

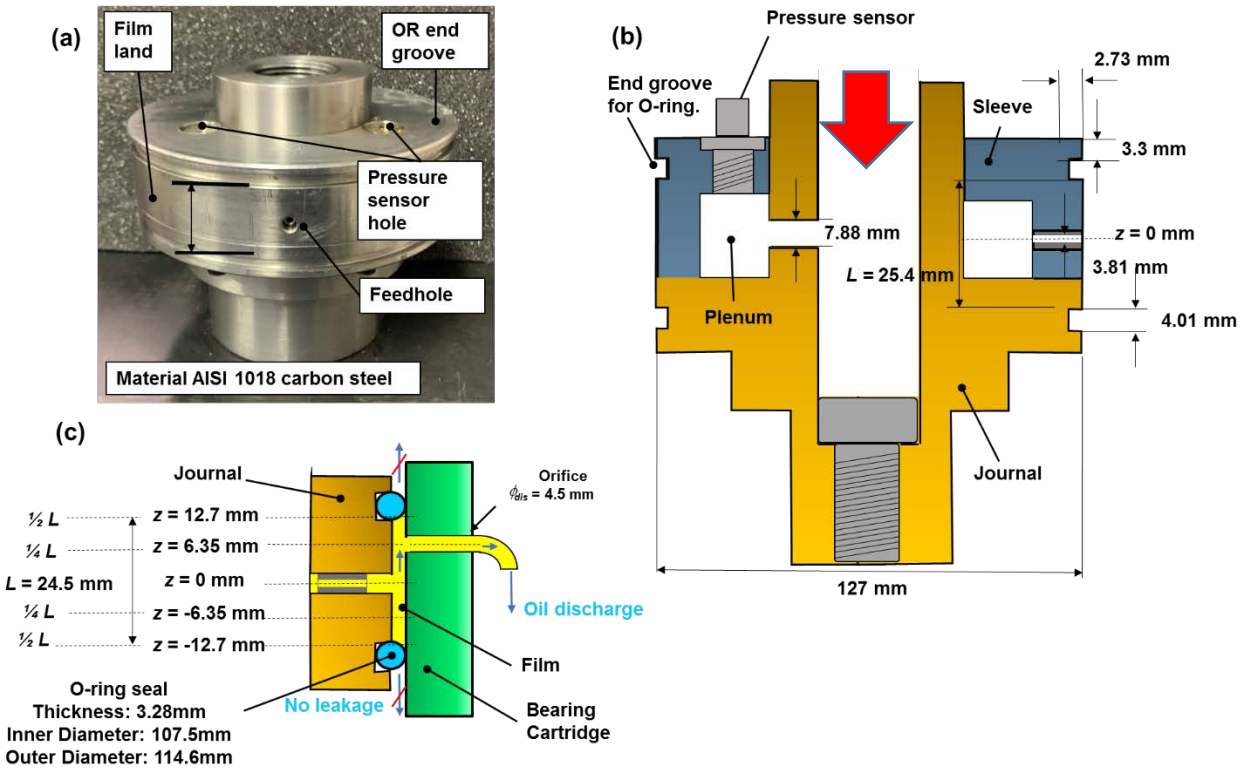

Fig. 4. (a) Photograph of test journal with end grooves and a feed hole, (b) schematic cross section view of journal with dimensions and (c) schematic cross-section view of journal and BC showing ORs installation with axial location of feedhole and discharge hole. (Drawings not to scale and exaggerated features)**.**

Figure 5 displays (a) the test journal showing the OR grooves, and (b) a section view in the journal, with groove and OR dimensions. The journal has two end grooves for installation of the O-rings. These grooves are 4.06 mm in width and 2.73 mm in depth. When inserted into the BC, the ORs installed in the journal push against the ID of the BC. The ORs selected are multipurpose Buna-N O-ring with an outer diameter of 114.6 mm and a thickness of 3.28 mm (AS568 standard O-ring size number 244), mounted on grooves with diameter of 121.2 mm. The groove depth and radial clearance comprise the groove gland depth, and with the groove width, make up the gland volume, as noted in the OR manufacturer handbook [9].

Two design parameters are carefully selected to ensure proper OR fit and sealing; namely OR squeeze and OR gland. The OR squeeze is the percentage of the OR thickness deformed after installation in the groove, while the gland fill is the percentage of the gland volume filled by the OR volume. If the squeeze and gland fill are too low, the OR will not seal; whereas an excessive squeeze and gland fill could permanently deform the seal; or worse yet, make the ORs overly stiff.

The OR and its groove dimensions satisfy manufacturer specifications for radial sealing, as stated in Ref. [9], to allow at least 80% gland fill (hence the larger groove width compared to the OR thickness), and no more than 25% squeeze.

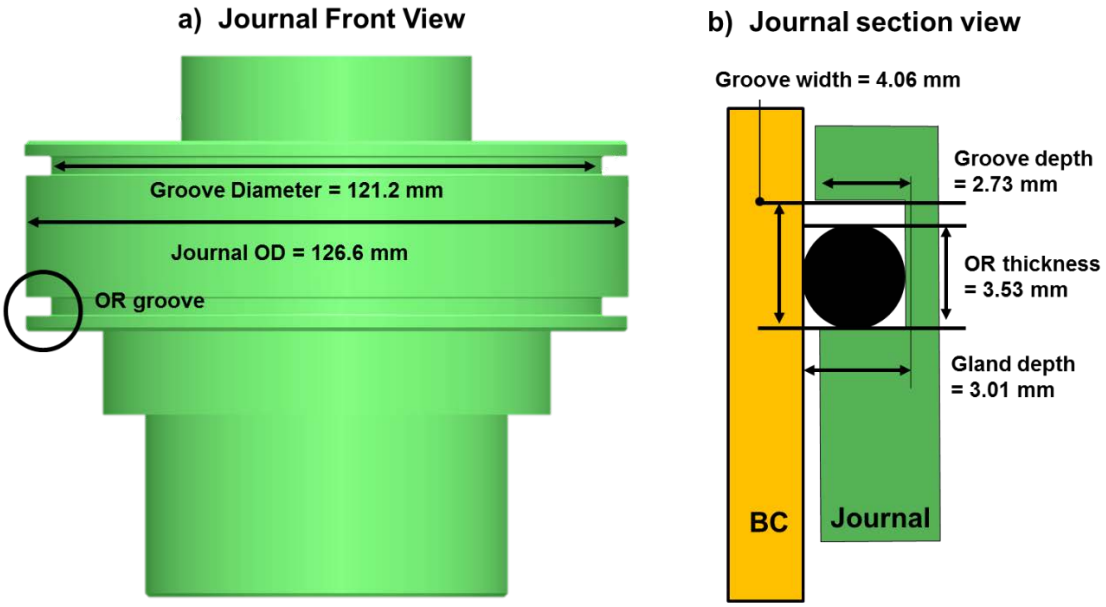

Fig. 5. Journal schematic views, (a) front view showing the groove and journal diameters, and (b) journal section view displaying groove and OR dimensions. (Figure not to scale, with exaggerated features).

A lubrication pump system circulates an ISO VG 2 lubricant through the test rig. The lubricant has density ρ = 780 kg/m^3 and viscosity μ = 3.06 mPa-s at 23^{o}C. The oil physical properties are similar to those of lubricants used in aircraft engines operating at a high temperature (T ~ 200^{o}C). Appendix B shows measurements of the lubricant physical properties.

A pump supplies lubricant into the journal, flows first into the filled in plenum and next into the film lands with sealed film lands. The lubricant exits the film through one discharge hole in the BC with location depicted in Fig 3(a). A pressure gauge and flow meter upstream of the journal measure the inlet pressure (P_S) and lubricant flowrate into the journal. The discharge hole connects to a suction line and pump that routes the oil through a bubble eliminator and into a 150 L storage tank. A relief valve limits the pressure in the supply line to a maximum pressure of 6.2 bar(g), when it opens and routes the oil back to the storage tank.

For an inlet pressure P_S = 0.7 bar(g), the average flowrate through the sealed ends SFD is 1.1 LPM. See Appendix C for measurements of the flow rate vs. supply pressure for the damper configured with open ends to ambient and ends sealed with the ORs.

Experimental Procedure and Identification of Force Coefficients[1]

The SFD parameter identification process begins by modeling the test damper as a two degree of freedom mechanical system undergoing lateral motions (X,Y). The identification method is common to obtain force coefficients from dynamic load tests [25]. Figure 6 displays an idealization of the structure mass (M_{BC}) as a point mass with springs (K's) and viscous dashpots (C's) that represent the contributions of the support structure, O-rings and squeeze film damper.

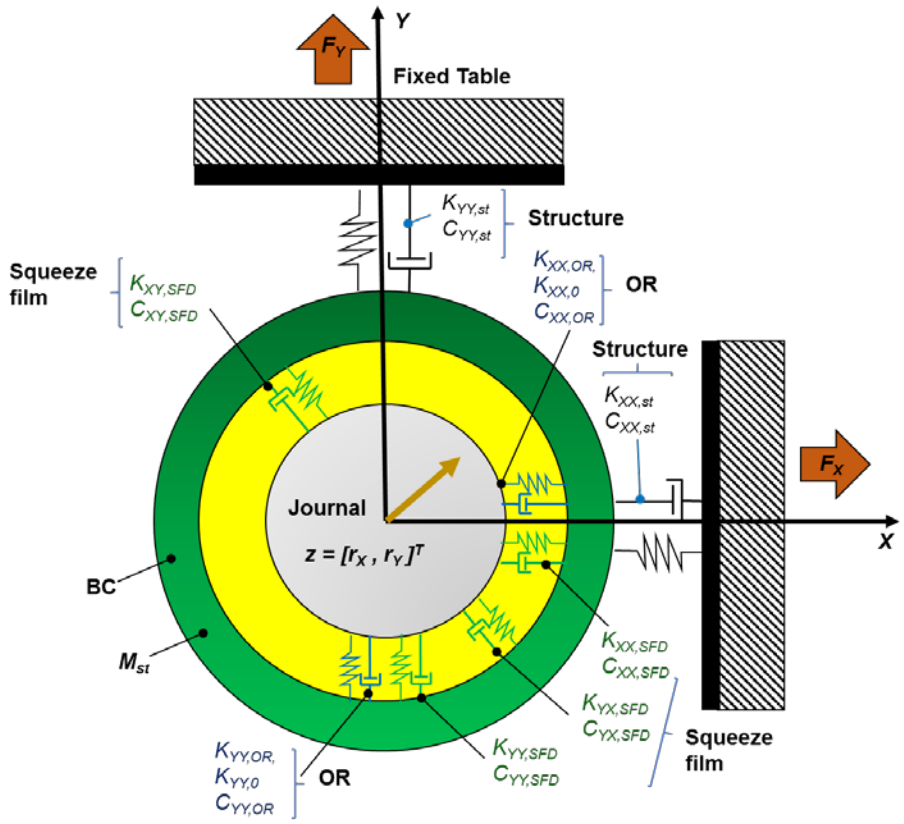

Fig. 6. Model of test rig for planar motions of a lumped mass (bearing cartridge) and force coefficients representing the actions of the squeeze film (SFD), support structure (*st*) and O-rings (ORs). Schematic view modified from Ref. [1].

The electromagnetic shakers deliver single frequency (ω) periodic forces $\mathbf{F}$=[F_X,F_Y] expressed as:

$$\mathbf{F}_{(t)} = \begin{bmatrix} F_X \\ F_Y \end{bmatrix} = F\,[1, \pm i]^T e^{i\omega t} = \overline{\mathbf{F}} e^{i\omega t} \tag{1}$$

[1] This section follows portions of the uncertainty analysis presented in Ref. [20]

where *i* denotes the imaginary unit. Note that F_X and F_Y are out of phase by 90° to produce circular orbit motions.

The BC with mass M_{BC} =15.2± 0.05 kg moves with acceleration $\mathbf{a} = [a_X, a_Y]^T = \bar{\mathbf{a}}\, e^{i\omega t}$, and its equation of motion is

$$M_{BC}\,\mathbf{a} = \mathbf{F}_{(t)} + \left[\mathbf{F}_{st} + \mathbf{F}_{OR} + \mathbf{F}_{SFD}\right] \tag{2}$$

where $\mathbf{F}_{st}$, $\mathbf{F}_{OR}$ and $\mathbf{F}_{SFD}$ are the reaction forces from the structure, the O-rings, and the squeeze film damper, respectively. The physical model for each of the elements in the test rig, i.e., the support structure, O-rings and squeeze film damper, follows the linearized model introduced by San Andrés and Koo [20]

$$\begin{aligned} -\mathbf{F}_{st} &= \mathbf{K}_{st}\,\mathbf{z} + \mathbf{C}_{st}\,\dot{\mathbf{z}} + \mathbf{M}_{st}\,\ddot{\mathbf{z}}, \\ -\mathbf{F}_{OR} &\sim \mathbf{K}_{OR}\,\mathbf{z} + \left(\mathbf{C} + \frac{1}{\omega}\mathbf{K}_0\right)_{OR}\dot{\mathbf{z}} \\ -\mathbf{F}_{SFD} &= \mathbf{C}_{SFD}\,\dot{\mathbf{z}} + \mathbf{M}_{SFD}\,\ddot{\mathbf{z}} \end{aligned} \tag{3}$$

where $\mathbf{z} = [r_X,\, r_Y]^T = \bar{\mathbf{z}}\; e^{i\omega t}$ is a vector of BC displacements relative to the journal (see Fig. 6). Above, (**K, C, M**) are 2x2 matrices of stiffness, damping and inertia force coefficients, i.e.,

$$\mathbf{K} = \begin{bmatrix} K_{XX} & K_{XY} \\ K_{YX} & K_{YY} \end{bmatrix},\ \mathbf{C} = \begin{bmatrix} C_{XX} & C_{XY} \\ C_{YX} & C_{YY} \end{bmatrix},\ \mathbf{M} = \begin{bmatrix} M_{XX} & M_{XY} \\ M_{YX} & M_{YY} \end{bmatrix} \tag{4}$$

Note $\mathbf{K}_{SFD} \sim 0$ as SFDs, in general, cannot generate a *true* static stiffness [1]. In addition, the O-rings include both a viscous damping coefficient as well as a quadrature stiffness $\mathbf{K}_0$ that represents material-like structural damping. These parameters are shown in Appendix D

During the experiments, sensors record the applied forces (**F**), the BC accelerations (**a**) and the displacements (**z**) relative to the journal and along the *X* and *Y* directions.

Using the Discrete Fourier Transform (DFT) brings Eq. (2) into the frequency domain as an algebraic equation for each (exerted) frequency (ω). That is, substituting $\mathbf{a}_{(t)} = \bar{\mathbf{a}}\, e^{i\omega t}, \mathbf{z}_{(t)} = \bar{\mathbf{z}}\, e^{i\omega t}, \mathbf{F}_{SFD} = \bar{\mathbf{F}}_{SFD}\, e^{i\omega t}$ into Eq. (2) gives

$$-\left[\bar{\mathbf{F}}_{st} + \bar{\mathbf{F}}_{OR} + \bar{\mathbf{F}}_{SFD}\right] = \bar{\mathbf{F}} - M_{BC}\,\bar{\mathbf{a}} \tag{5}$$

Since,

$$
\begin{aligned}
-\overline{\mathbf{F}}_{st} &= \left(\mathbf{K}_{st} + \mathbf{C}_{st} - \omega^2 \mathbf{M}_{st}\right)\overline{\mathbf{z}} \\
-\mathbf{F}_{OR} &\sim \left(\mathbf{K}_{OR} + i\,\mathbf{K}_0 + i\,\omega\,\mathbf{C}_{OR}\right)\overline{\mathbf{z}} \\
-\mathbf{F}_{SFD} &= \left[i\omega\,\mathbf{C}_{SFD} - \omega^2 \mathbf{M}_{SFD}\right]\overline{\mathbf{z}}
\end{aligned}
\tag{6}
$$

Then, Eq. (5) becomes

$$
\left\{\left[\mathbf{K}_{st} + \mathbf{K}_{OR} + i\,\mathbf{K}_0 - \omega^2\left(\mathbf{M}_{st} + \mathbf{M}_{SFD}\right)\right] + i\,\omega\left[\mathbf{C}_{st} + \mathbf{C}_{OR} + \mathbf{C}_{SFD}\right]\right\}\overline{\mathbf{z}} = \left(\overline{\mathbf{F}} - M_{BC}\,\overline{\mathbf{a}}\right) \tag{7}
$$

Or written in a succinct form as

$$
\mathbf{H}_{L_{(\omega)}}\,\overline{\mathbf{z}} = \overline{\mathbf{F}} - M_{BC}\,\overline{\mathbf{a}} \tag{8}
$$

where $\mathbf{H_L}$ represents the complex dynamic stiffness of the test system and that includes the physical parameters from the elastic support structure, the O-rings and the squeeze film damper;

$$
\mathbf{H}_{\mathbf{L}_{(\omega)}} = \left[\mathbf{K}_{st} + \mathbf{K}_{OR} + i\,\mathbf{K}_0 - \omega^2\left(\mathbf{M}_{st} + \mathbf{M}_{SFD}\right)\right] + i\,\omega\left[\mathbf{C}_{st} + \mathbf{C}_{OR} + \mathbf{C}_{SFD}\right] \tag{9a}
$$

$$
\mathbf{H}_L = \left[\mathbf{K}_L - \omega^2\mathbf{M}_L + i\,\omega\,\mathbf{K}_{0,OR} + i\omega\,\mathbf{C}_L\right] \tag{9b}
$$

where

$$
\mathbf{K}_L = \left(\mathbf{K}_{st} + \mathbf{K}_{OR}\right),\ \mathbf{M}_L = \left(\mathbf{M}_{SFD} + \mathbf{M}_{st}\right),\ \mathbf{C}_L = \left(\mathbf{C}_{st} + \mathbf{C}_{OR} + \mathbf{C}_{SFD}\right) \tag{10}
$$

Above $(\mathbf{K}, \mathbf{C}, \mathbf{M})_L$ are matrices containing the stiffness, damping and added mass coefficients of the lubricated system.

Multiple experiments over a prescribed set of frequencies and producing clockwise and counter clockwise orbital motions produce enough information to fully determine the elements of $\mathbf{H}_L$, the complex dynamic stiffness of the lubricated system. The real part of Eq. (9b) $\mathrm{Re}(\mathbf{H}_L) \rightarrow (\mathbf{K}_L - \omega^2\,\mathbf{M}_L)$ delivers the lubricated system stiffness ($\mathbf{K}_L$) and added mass ($\mathbf{M}_L$), while the imaginary part $\mathrm{Im}(\mathbf{H}_L) \rightarrow (\omega\,\mathbf{C}_L)$ estimates the lubricated system damping ($\mathbf{C}_L$).

The Instrumental Variable Filter (IVF) method [22], an extension of a least squares algorithm, finds the best parameters fitting the model $\mathrm{Re}(\mathbf{H}_L) \rightarrow (\mathbf{K}_L - \omega^2\mathbf{M}_L)$ and $\mathrm{Im}(\mathbf{H}_L) \rightarrow (\omega\,\mathbf{C}_L)$. The IVF method minimizes the approximation errors from measurement noise, thus leading to a consistent estimation of the damper parameters.

In the experimental procedure, the support structure force coefficients $(\mathbf{K}, \mathbf{C}, \mathbf{M})_{st}$ are first obtained with a dry system (without any lubricant) and without the O-rings installed. Appendix D details the identification procedure of the dry structure force coefficients.

Next, still with a dry structure and with the O-rings installed in the journal and pressing against the BC, a new set of applied single frequency forces produces BC periodic motions with amplitude r = 0.1c, r = 0.15c and r = 0.2c. The dynamic loads, clockwise (+ω) and counter clockwise (-ω), have a frequency (ω) = 10 Hz, 20 Hz to 70 Hz

Test results with a sealed journal in a dry condition produce a complex stiffness matrix of the form

$$\mathbf{H}_{st+OR_{(\omega)}} = \left[\mathbf{K}_{st} + \mathbf{K}_{OR} + i\,\mathbf{K}_0 - \omega^2\mathbf{M}_{st}\right] + i\,\omega\left[\mathbf{C}_{st} + \mathbf{C}_{OR}\right] \tag{11}$$

and from which the O-rings representative force coefficients $(\mathbf{K}, \mathbf{K_0}, \mathbf{C})_{OR}$ follow. See Appendix D.

Lastly, lubricant is supplied into the clearance of the SFD at a set pressure P_S=0.7 bar(g) and the single-frequency dynamic load tests repeat to record forces, BC displacements and accelerations. The experimental results deliver $(\mathbf{K}, \mathbf{C}, \mathbf{M})_L$ and the SFD force coefficients are

$$\mathbf{C}_{SFD} = \mathbf{C}_L - \left(\mathbf{C}_{st} + \mathbf{C}_{OR}\right);\ \mathbf{M}_{SFD} = \mathbf{M}_L - \mathbf{M}_{st} \tag{12}$$

It is important to realize the shakers have a peak load capacity of 2,200 N hence limiting the amplitude of the BC tangential speed $v_s = (r\omega)$, also known as a squeeze velocity. For the largest amplitude (r) and excitation frequency (ω), the peak v_s = 24.5 mm/s and the largest squeeze film Reynolds number $Re_S = (\rho/\mu)\omega c^2 = 8.8$.

As a reference for the SFD force coefficients shown next, a tightly sealed SFD operating with small amplitude circular centered orbits produces viscous damping (C^*) and added mass (M^*) coefficients equal to [19]:

$$C^* = 12\pi\mu L\left(\frac{D}{2c}\right)^3 = 34.4\,\text{kN-s/m}\ \ ;\ \ M^* = \rho\frac{\pi L}{c}\left(\frac{D^3}{2}\right) = 57\,\text{kg} \tag{13}$$

The analytical coefficients C^* and M^* are valid only for Re_S < 10 and operation with a full film and no oil cavitation or air ingestion

Experimental Results

This section presents the experimental results derived from the whirl orbits produced by periodic load excitations on the ORs sealed ends damper. The average radial clearance between the journal OD and the BC ID is c=279 μm +/- 6 μm for all the experiments.

The (structure + OR) force coefficients are first obtained from tests with a *dry* (no lubricant) system. One rig configuration has no ORs (open ends) and the other has the ORs installed. Refer to Appendix D for details on the identification process of the dry (unlubricated) structure. The Tables below list the experimentally estimated force coefficients and include confidence intervals derived from the uncertainty in the measurements. Appendix E presents a detailed procedure on the quantification of uncertainty for the experimental apparatus.

Structure force coefficients

Table 2 shows the dry structure parameters obtained from circular orbits with orbit amplitude r/c = 0.05 and over a frequency range ω = 30 – 120 Hz. Note the test rig structure is slightly orthotropic and its damping ratio is just ~ 2%.

Table 2. Structure physical parameters for dry (without lubricant) structure obtained from circular orbit tests. Parameters identified in the frequency range from 30 to 120 Hz. Orbit amplitude r/c = 0.05 and static eccentricity e_s/c = 0.0. M_{BC}=15.2 kg.

Structural parameter		Direct		Cross-coupled	
		XX	***YY***	***XY***	***YX***
Stiffness	K_{st} [MN/m]	17.8 ± 0.8	16.8 ± 0.7	-0.30	0.10
Mass	M_{st} [kg]	3.5 ± 0.4	1.1 ± 0.1	0.02	-0.40
Damping	C_{st} [kN-s/m]	0.6 ± 0.04	0.4 ±0.02	-0.10	-0.04
Natural Frequency	$f_{n,st}$ [Hz]	172 ± 1.0	167 ±1.0	$f_{n,st} = \sqrt{\frac{K_{st}}{M_{BC}}}$	
Damping Ratio	ζ_{st} [-]	0.02	0.02	$\zeta_{st} = C_{st} / 2\sqrt{K_{st} M_{BC}}$	

Force coefficients for structure with O-rings

Table 3 lists the force coefficients for the dry structure with O-rings installed. The test conditions for identification are similar to those for the structure alone. Note the structure + ORs system remains isotropic albeit showing much larger direct stiffnesses, about a 45% increase, and

a nearly 4.5 times increase in damping coefficients that lead to a raise in the system damping ratio to ~ 6% (average). The O-rings thus produce a remarkable increase in stiffness and damping coefficients thus raising the system natural frequency.

Table 3. Structure plus O-rings physical parameters for dry (without lubricant) structure obtained from circular orbit tests. Parameters identified in the frequency range from 30 to 120 Hz. Orbit amplitude *r/c* = 0.05 and static eccentricity e_s/c = 0.0. M_{BC}=15.2 kg.

parameter		Direct		Cross-coupled	
		XX	***YY***	***XY***	***YX***
Stiffness	K_{st+OR} [MN/m]	25.9 ± 1.1	24.7 ± 1.1	-0.40	-0.90
Mass	M^*_{st+OR} [kg]	1.4 ± 0.1	0.7 ± 0.1	-0.40	-0.40
Damping	C_{st+OR} [kN-s/m]	2.7 ± 0.2	1.9 ± 0.2	-0.02	0.20
Quadrature Stiffness	$K_{0,OR}$ [MN/m]	2.3 ± 0.1	2.4 ± 0.1	0.03	-0.10
Natural Frequency	$f_{n,st+OR}$ [Hz]	208 ± 2.0	203 ± 2.0	$f_{n,st+OR}=\sqrt{\frac{K_{st+OR}}{M_{BC}}}$	
Damping Ratio	ζ_{st+OR} [-]	0.07 ± 0.01	0.05 ± 0.01	$\zeta_{st+OR}=\frac{C_{st+OR}}{2\sqrt{K_{st+OR}M_{BC}}}$	

Estimated experimental force coefficients for O-rings.

Note the ORs' force coefficients follow from $(K,C)_{OR}=(K,C)_{st+OR}-(K,C)_{st}$. The identification assumes that the physical behavior of the O-rings follows Eq. (3), i.e., with frequency independent stiffness (K) and *viscous-like* damping (C) coefficients. See Figure D.1 for a depiction of the test system complex stiffnesses vs. frequency.

Table 4 shows the identified force coefficients for the pair of ORs installed in the rig. Note the ORs quadrature stiffness (K_0) is representative of a physical effect at a low frequency that reveals a structural-like damping. That is $(K_0/K)=\gamma \sim 0.26$ can be construed as a material loss factor.

Table 4. ORs estimated force coefficients obtained from circular orbit tests. Parameters identified in the frequency range from 30 to 120 Hz. Orbit amplitude *r/c* = 0.05 and static eccentricity e_s/c = 0.0

OR force coefficients		Direct coefficients		Cross-coupled	
		XX	***YY***	***XY***	***YX***
Stiffness	K_{OR} [MN/m]	8.1 ± 0.4	7.9 ±0.4	-0.1	-1.0
Damping	C_{OR} [kN-s/m]	2.1 ± 0.1	1.5 ± 0.1	-0.4	0.0
Quadrature Stiffness	$K_{0,OR}$ [MN/m]	2.3 ± 0.1	2.0 ± 0.1	.0.1	0.2

Complex stiffnesses for lubricated test system

With the structure and installed ORs properly identified, dynamic load experiments continued with the test system lubricated with the ISO VG2 oil supplied at a low pressure (P_S=0.7 bar(g)). The range of whirl frequencies only extends to 70 Hz as the SFD produced significant reaction forces (damping and inertial) and the external shakers have a limit low capacity.

Figure 6 depicts the real and imaginary parts of the lubricated system dynamic stiffness, Re(H_{XX}, H_{YY})$_L$ and Ima(H_{XX}, H_{YY})$_L$, versus whirl frequency (ω) and orbits with amplitude *r/c* = 0.1. The symbols (squares and circles) denote the experimentally derived complex stiffness, whereas the dotted lines represent the best curve fit of the physical model to the test data. The inset table list the correlation factors (R^2) of the measured data to the curve fits. Similarly, Figures 7 and 8 show both components of $\mathbf{H}_L$, with curve fits of the physical model and correlation factors (R^2), for tests with an orbit radius *r/c* = 0.15 and *r/c* = 0.2, respectively.

In Figs. 6 to 8, the intercepts of the real part of $\mathbf{H}_L$ with the vertical axis show direct stiffness (K) magnitudes that approximate those of the dry test system(structure+ORs). The inset tables in Figs. 6-8 show a good correlation factor of Re($\mathbf{H}_L$) with the physical model force coefficients defined by (K, C, M)$_L$. Incidentally, realize Re($\mathbf{H}_L$) quickly decreases with frequency to reveal large fluid inertia effects from the squeeze film.

In case of the imaginary part of $\mathbf{H}_L$, the inset tables in Figs. 6-8 show a good correlation factor $R^2 > 0.9$. Additionally, Figs. 6-8 include Im($\mathbf{H}_{st+OR}$) to showcasing the ORs + structure quadrature stiffness and damping. Compared to Im($\mathbf{H}_{st+OR}$), note that the slope of Im($\mathbf{H}_L$) is considerably higher, thus evidencing a dominant viscous damping from the squeezed oil film during the tests.

Incidentally, Im($\mathbf{H}_L$) also displays a quadrature stiffness ($K_{0,L}$), similar magnitude, compared to the magnitude seen with the dry system ($K_{0,st+OR}$). This happenstance demonstrates that the effects of the structural-like damping in the ORs persist in the damping of the lubricated system, albeit the viscous damping in the film (ωC) remains as the predominant source of energy dissipation for the lubricated system.

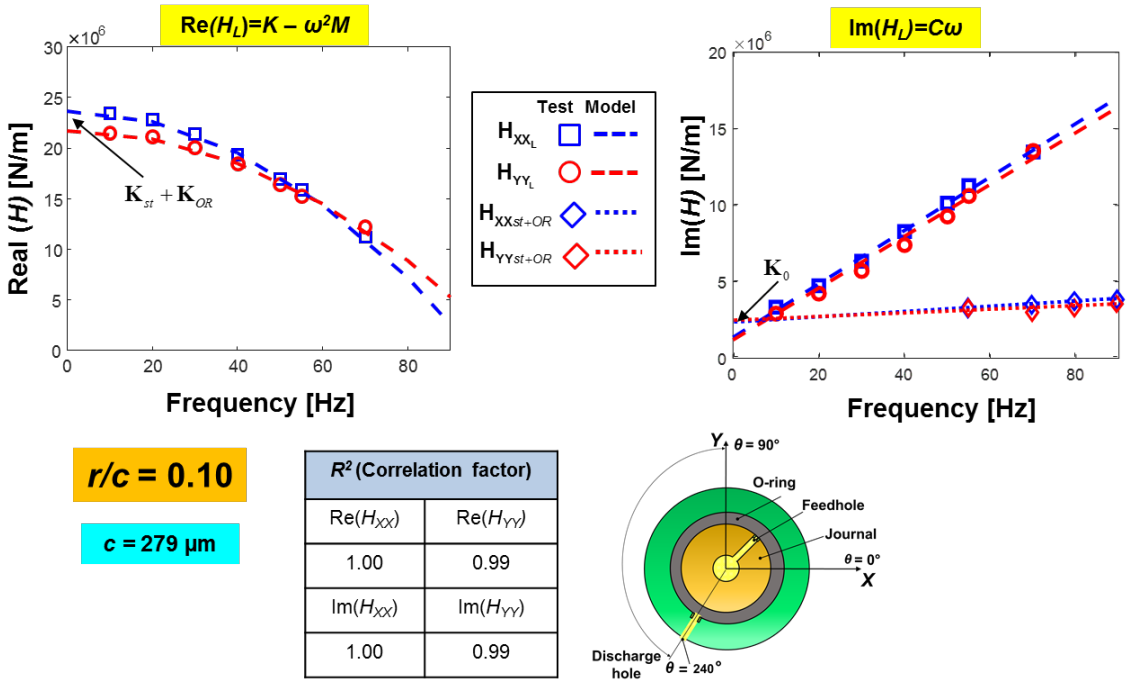

Fig. 6. Real and imaginary parts of direct complex dynamic stiffness (H_{XX}, H_{YY})$_L$ vs. whirl frequency. ORs sealed ends damper. Lubricated test system with P_S = 0.7 bar(g). Circular centered orbits with amplitude r/c = 0.10 (e_s = 0.0) and frequency ω= 10 – 70 Hz. Lubricant supplies through one feedhole (θ= 45º, z = 0).

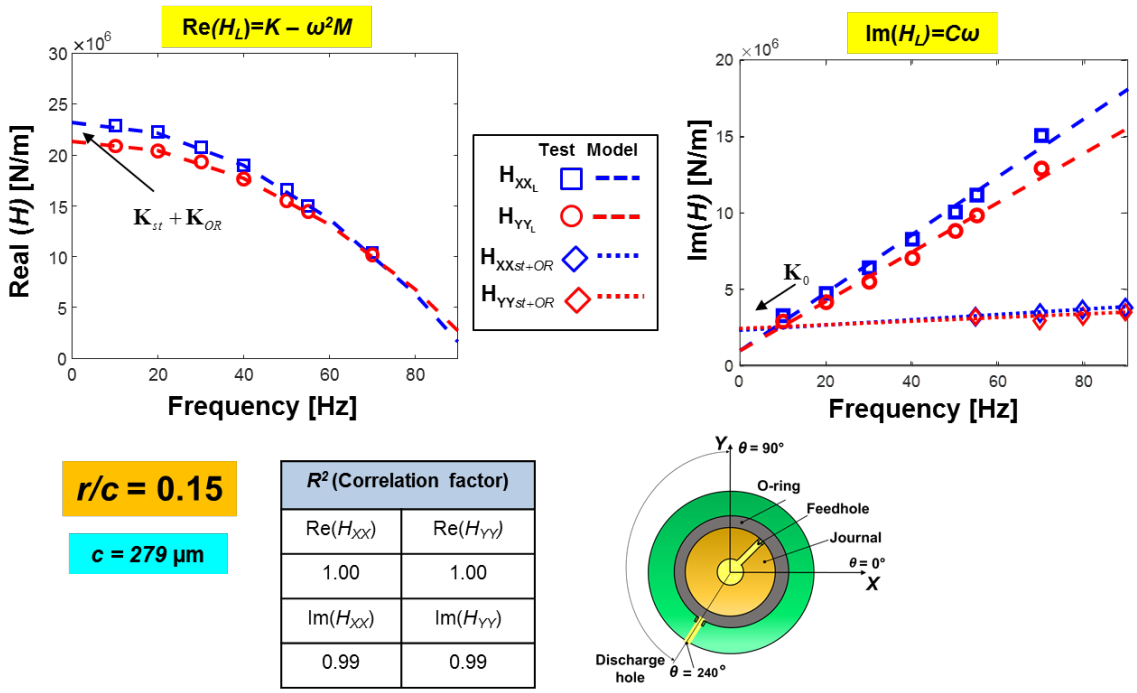

Fig. 7. Real and imaginary parts of direct complex dynamic stiffness (H_{XX}, H_{YY})$_L$ vs. whirl frequency. ORs sealed ends damper. Lubricated test system with P_S = 0.7 bar(g). Circular centered orbits with amplitude r/c = 0.15 (e_s = 0.0) and frequency ω = 10 – 70 Hz. Lubricant supplies through one feedhole (θ = 45º, z = 0).

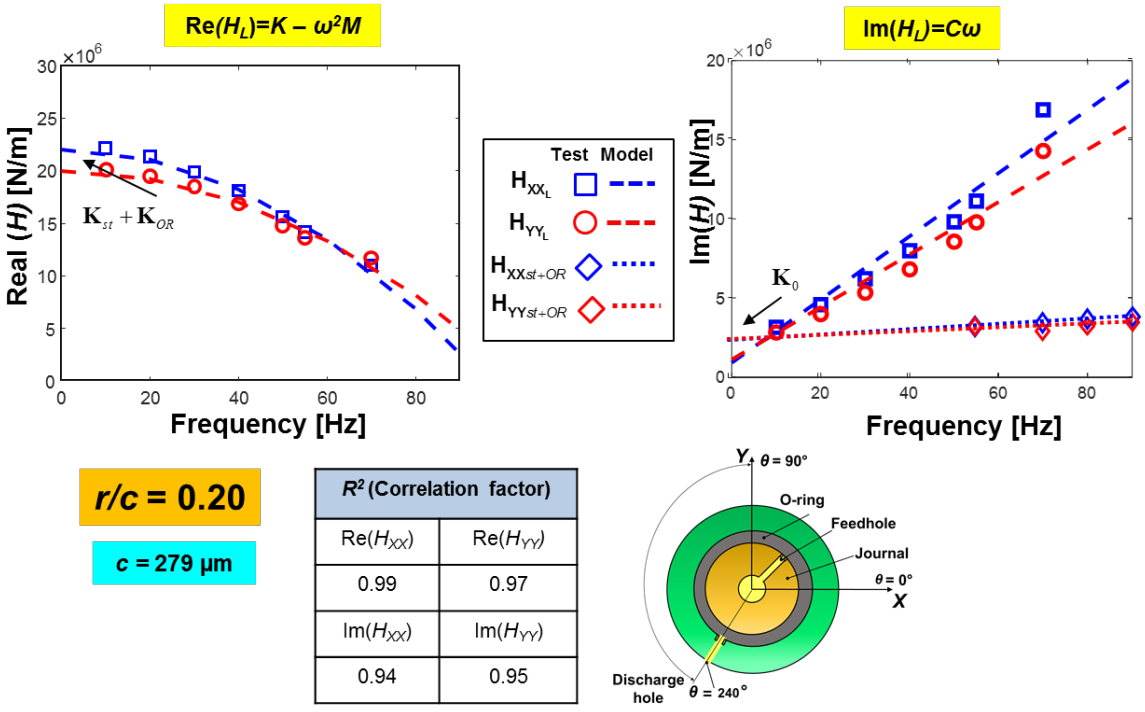

Fig. 8. Real and imaginary parts of direct complex dynamic stiffness (H_{XX}, H_{YY})$_L$ vs. whirl frequency. ORs sealed ends damper. Lubricated test system with P_S = 0.7 bar(g). Circular centered orbits with amplitude r/c = 0.20 (e_s = 0.0) and frequency range ω= 10 – 70 Hz. Lubricant supplies through one feedhole (θ= 45º, z = 0).

Table 5 summarizes the lubricated system estimated force coefficients, derived from tests presented in Figs. 6-8, and confidence intervals for the identified parameters from the uncertainty in the measurements. The identified stiffness coefficients (K_L) show the same magnitude as the stiffness coefficients estimated with a dry system (K_{st+OR}), thus showing that K_{SFD} ~0.

In the case of the inertia coefficients for the lubricated system (M_L), their magnitudes are at least 3 times larger than the BC mass (M_{BC}=15.2 kg). The fluid film inertia effect is so large that the system natural frequnecy has dropped to just 90 Hz, whereas it was ~ 200 Hz for the dry system (structure + ORs). Similarly, the viscous damping coefficients in the lubricated system are at least one order of magnitude larger, compared to those from the equivalent viscous damping for the (dry) structure + ORs. Note that the estimated force coefficients for the lubricated system show a near constant magnitude, independent of the orbit radius (r/c) when considering the uncertainty of the dentfiied parameters. Thus, the system natural frequency does not change as r/c grows. This is also the case for the system damping ratio, with average magnitude of ζ_L= 0.4, nearly 6.6 times larger than that of the (dry) structure + ORs (ζ_{st+OR} = 0.06).

Table 5. Lubricated System: experimental force coefficients estimated from circular centered orbits (e_s = 0.0) with orbit amplitude r/c= 0.1, 0.15 and 0.20 and over frequency range ω= 10 – 70 Hz. Test system lubricated with P_S=0.7 bar(g).

	Stiffness K_L [MN/m]		**Inertia M_L** [kg]		**Damping C_L** [kN-s/m]		**Quadrature Stiffness, $K_{0,L}$** [MN/m]	
r/c	***XX***	***YY***	***XX***	***YY***	***XX***	***YY***	***XX***	***YY***
0.10	23.6 ± 1.1	21.7 ± 0.9	65.0 ± 8.6	51.0 ± 6.9	27.8 ± 2.1	27.1 ± 2.0	1.4 ± 0.1	1.0 ± 0.1
0.15	23.2 ± 1.0	21.3 ± 1.0	66.6 ± 8.8	57.5 ± 7.5	30.2 ± 2.2	25.8 ± 2.0	1.0 ± 0.1	1.0 ± 0.1
0.20	22.0 ± 1.0	20.0 ± 0.9	60.0 ± 7.9	46.5 ± 6.1	31.3 ± 2.3	26.4 ± 2.0	1.2 ± 0.1	0.9 ± 0.1

Force coefficients for SFD (only)

Table 6 summarizes the estimated SFD coefficients, from subtracting the coefficients identified with a dry structure + ORs, as seen in Eq. 12. The measurements show orthotropy in the

system, likely due to the connections to sensors and various inlet/outlet lubricant lines. The identified SFD stiffness coefficients $K_{SFD} \sim 0$ and remain constant within the uncertainty bands. With respect to derived added mass coefficients, they show up to four times M_{BC}=15.2 kg for tests with the smallest size orbit (r/c=0.05), and remain largely unchanged since the remnant structure + ORs coefficients, on average, are no larger than two kilograms (M^{*}_{st+OR}). Note that the change in the magnitude of M_{SFD} with increasing orbit radius falls within the uncertainty in the measurements, thus remaining with a constant magnitude. As for damping coefficients, they show a ~10% decrease in magnitude by removing C_{st+OR}, and also stay constant with increasing r/c.

Figure 9 displays the dimensionless SFD damping and added mass coefficients, $\underline{C}_{SFD} = C_{SFD} / C^{*}$, $\underline{M}_{SFD} = M_{SFD} / M^{*}$ vs. orbit radius r/c. The normalized damping coefficients $\underline{C}_{SFD} \sim 0.7C^{*}$ as $r/c \rightarrow 0$, thus showing that the prediction for a (full film) tightly sealed damper does not agree with the experimentally derived coefficients. The difference is likely due to oil vapor cavitation (see Appendix G). The added mass coefficients $\underline{M}_{SFD}$ range from $0.8M^{*}$ to $1.1M^{*}$ and agree better with the analytical formula prediction.

Table 6. Sealed ends SFD: experimental force coefficients estimated from circular centered orbits (e_s = 0.0) with orbit amplitude r/c= 0.1, 0.15 and 0.20 and over frequency range ω= 10 – 70 Hz. Test system lubricated with P_S=0.7 bar(g).

	Stiffness K_{SFD} [MN/m]		**Inertia M_{SFD}** [kg]		**Damping C_{SFD}** [kN-s/m]	
r/c	***XX***	***YY***	***XX***	***YY***	***XX***	***YY***
0.10	-2.3 ± 2.1	-3.0 ± 2.0	63.6 ± 8.7	50.3 ± 7.0	25.1 ± 2.2	25.2 ± 2.1
0.15	-2.7 ± 2.0	-3.4 ± 2.1	65.2 ± 8.9	56.8 ± 7.2	27.5 ± 2.3	23.9 ± 2.0
0.20	-3.9 ± 2.1	-4.7 ± 2.0	58.6 ± 8.0	45.8 ± 6.2	28.6 ± 2.4	24.5 ± 2.1

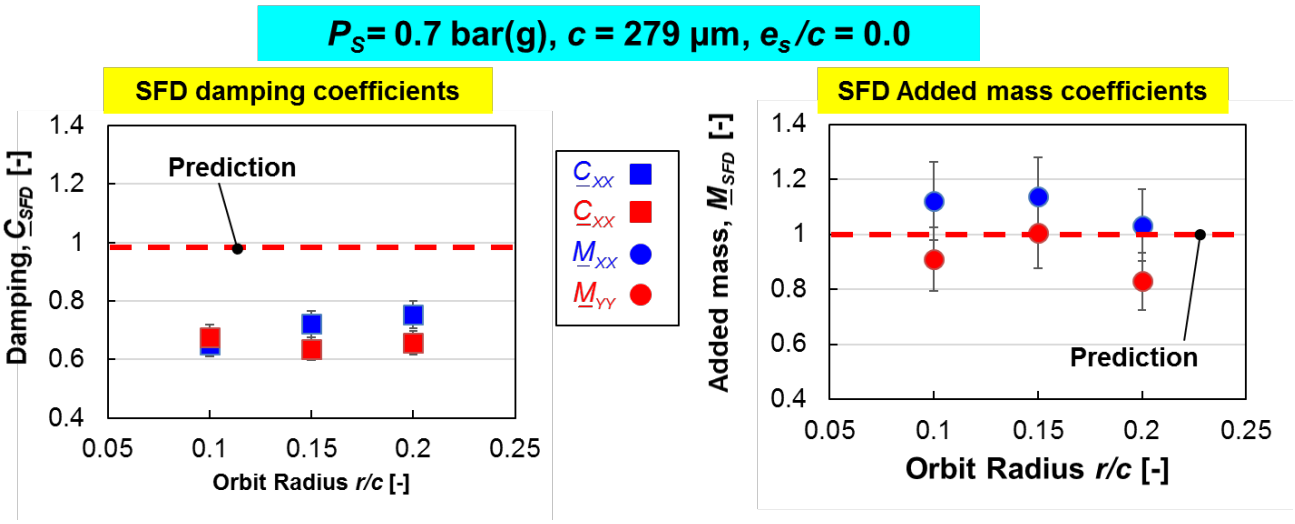

Fig. 9. ORs sealed ends damper: damping ($\underline{C}_{SFD}$) and inertia ($\underline{M}_{SFD}$) coefficients vs. orbit radius (r/c). Lubricated test system with P_S = 0.7 bar(g). Estimated parameters from CCO (e_s = 0) and frequency range ω = 10 – 70 Hz. Lubricant supplied through one feedhole (θ= 45º, z = 0).

The current findings produce damping coefficients about 10% lower than prior experimental results obtained in the same test facility albeit conducted with lubricant supplied at a high supply pressure (6.9 bar); see San Andrés et al. [23]. Incidentally, Ref. [22] reports that damping coefficients from an ORs end sealed SFD increase by nearly 10% when accounting for the viscous damping provided by the O-rings. This is also the case in the current experimental results.

Lastly, the estimated cross-coupled coefficients $(K, C, M)_{XY}$ and $(K, C, M)_{YX}$ are at least one order or magnitude smaller than the direct force coefficients. Hence, the cross-coefficients do not affect the performance of the test SFD. Refer to Appendix F for details on the identified cross-coupled coefficients.

Measurements of applied load vs squeeze velocity

In the tests, the electromagnetic shakers deliver periodic loads, 90º out of phase, in the X and Y directions, to produce centered whirl orbits with radii r=0.10c. r=0.15c and r=0.20c and for a range of excitation frequencies (70 Hz max.). Consider K_{avg} = 22 MN/m, M_{avg} =73 kg and C_{avg} = 28 kN-s/m as (average) force coefficients for the lubricated system coefficients, see Table 5. Note that M_{avg} includes the BC mass.

Note that $F_{est} \sim r\,|K_{avg} - M_{avg}\,\omega^2 + i\,C_{avg}\,\omega|$ is a representation of the force delivered by a shaker to produce circular orbits with amplitu r . Figure 10 displays F_{est} and the actual delivered force F_{app} vs. frequency. $F_{app,}$ in Fig. 10 is the average from the X and Y load amplitudes. The correlation between F_{app} and F_{est} is rather good, thus denoting the identified force coefficients are accurate.

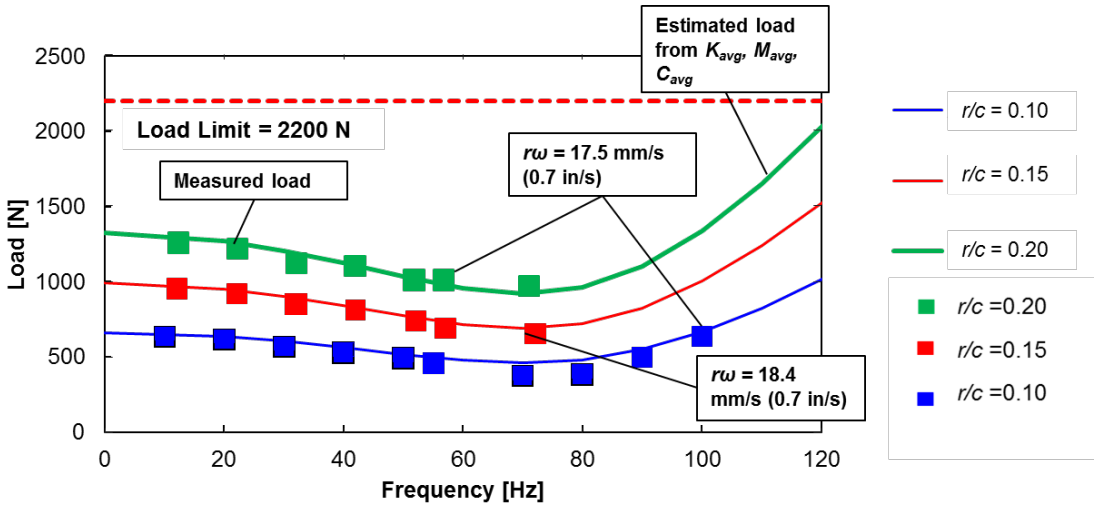

Fig. 10. Lubricated System: applied (shaker) load F_{app} and estimated force F_{est} vs. excitation frequency ω. Recorded loads over the frequency range ω= 10 – 100 Hz. Oil supply pressure P_S=0.7 bar(g).

Dynamic pressure measurements within oil delivery plenum in journal

A check valve in the journal feedhole reduces backflow, while the journal plenum is filled with oil. A piezoelectric pressure sensor records the dynamic pressure in the oil plenum inside the journal and in order to certify the check valve adequate operation, see Fig. 3(a). Fig. 11 shows recorded peak to peak dynamic pressures within the oil plenum vs. excitation frequency and for orbit radii r/c = 0.10, 0.15 and 0.20. The peak-to-peak pressures though not nil, are proportional to the whirl frequency and not a function of the orbit radius. This shows that even with a check valve, oil backflow is still present. Importantly enough, at 120 Hz the highest pk-pk pressure in the plenum is about 0.6 bar, similar in size to the supply pressure. Operation at a higher frequency may cause the oil to release its gaseous content or worse yet suction air into the plenum.

See Appendix F for measurements of the dynamic pressure profile in the film lands, measurements of the film thickness (h) and peak-to-peak dynamic pressures in the film lands.

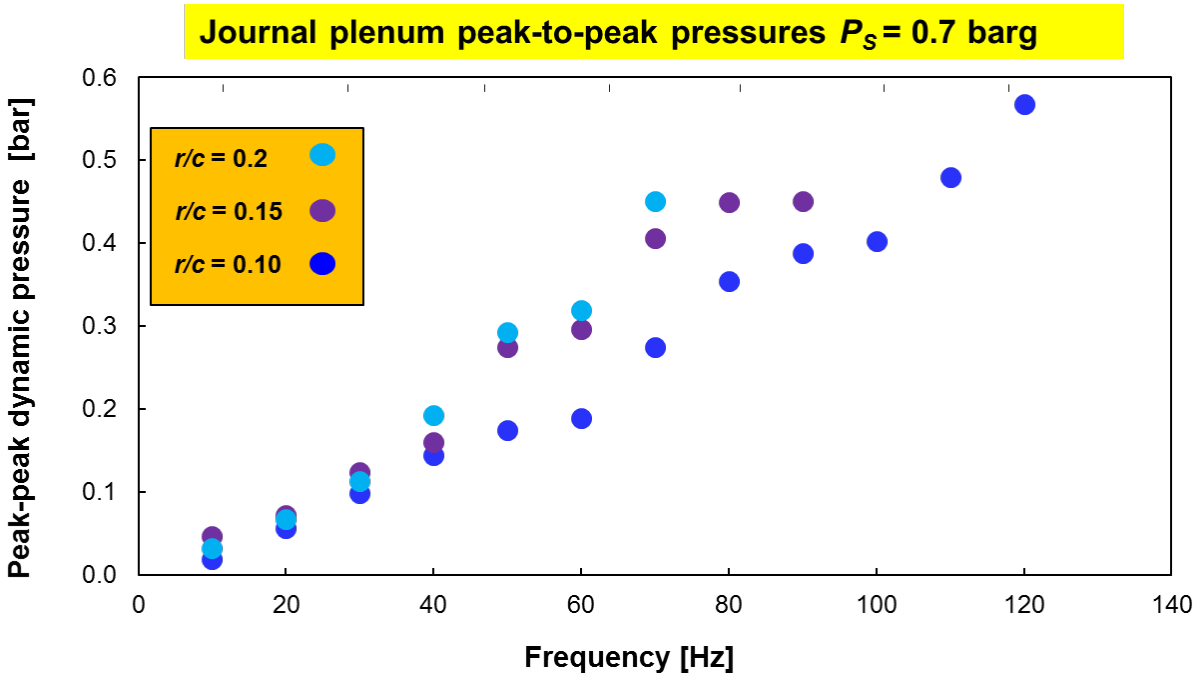

Fig 11. ORs sealed damper P_S=0.7 bar(g). Recorded peak-to-peak dynamic pressures inside the journal plenum versus frequency. Circular entered orbits with frequency ω = 10 Hz to 120 Hz, with radius r/c = 0.2

Conclusions

This report details measurements of the dynamic forced response of a short-length SFD (L/D = 0.2) sealed with O-rings. The lubricant, ISO VG 2, with supply pressure P_S=0.7 barg flows though one check-valve into the squeeze film land. The lubricant exits through one hole midway between the damper feedhole and one O-ring. Single frequency loads produce circular centered orbits with radii r/c = 0.10, 0.15 and 0.20. The parameter identification estimates force coefficients in the frequency range from 10 Hz to 70 Hz. The major findings are:

a) The ORs identified force coefficients, demonstrate frequency independence in the selected frequency range. The ORs stiffness (K_{OR}) is sizable, about ½ of the elastic rods' structural stiffness. The ORs also shows a quadrature stiffness $K_{0,}$ such that (K_0/K_{OR}) ~ 0.26 reveals a significant material loss factor. The OR viscous damping is also significant and contributes to about 10% of the damping of the lubricated system. The squeeze film lands produce the other 90% damping.

b) The identified SFD force coefficients show a near constant magnitude with increasing orbit radius (r/c). The added mass or fluid inertia (M_{SFD}) is so large that the system natural frequency drops from ~200 Hz (structure +ORs) to 90 Hz. The experimental force coefficients, C_{SFD} ~ 0.7C* and M_{SFD} ~ 1.1 M^*, moderately agree with predictions for a fully sealed SFD. The discrepancy in viscous damping is likely due to oil vapor cavitation and air entrainment into the film lands.

c) Measurements of the dynamic peak-to-peak pressure in the plenum upstream of the check valve show pressure fluctuations with magnitude proportional to the whirl frequency.

d) The dynamic pressure profiles in the film lands show a steady rise in peak-to-peak magnitude as the squeeze velocity ($r\omega$) grows. The pressure profiles show flat low-pressure zones as the film gap increases, and spikes plus rugged multiple peak pressure zones for $v_s = r\omega$ > 21 mm/s. The pressure waves demonstrate both oil vapor cavitation and air entrainment in the film lands.

References

[1] San Andrés, L., 2010, *Modern Lubrication Theory*, "Squeeze Film Dampers," Notes 13, Texas A&M University Digital Libraries, [Mar 30, 2020], http://oaktrust.library.tamu.edu/handle/1969.1/93253.

[2] Miyachi, T., Hoshiya, S., Sofue, Y., Matsuki, M., and Torisaki, T., 1979 , "Oil Squeeze Film Dampers for Reducing Vibration of Aircraft Gas Turbine Engines," ASME Paper No. 79-GT-133, https://doi.org/10.1115/79-GT-133 .

[3] Gehannin, J., and Arghir, M., 2010, "Complete Squeeze-Film Damper Analysis Based on the "Bulk Flow" Equations," Tribol. Trans., 53(1), pp. 84–96, https://doi.org/10.1080/10402000903226382 .

[4] Leader, M. E., Whalen, J. K., and Grey, G. G., 1995, "The Design and Application of a Squeeze Film Damper Bearing to a Flexible Steam Turbine Rotor,"24th Turbomachinery Symposium, College Station, TX, pp. 49–58, https://doi.org/10.21423/R1R36D

[5] Bansal, P. N., and Hibner, D. H., 1978, "Experimental and Analytical Investigation of Squeeze Film Bearing Damper Forces Induced by Offset Circular Whirl Orbits," ASME J. Mech. Design, **100**(3), pp. 549-557, https://doi.org/10.1115/1.3453967 .

[6] Zeidan, F., San Andrés L., and Vance, J., 1996, "Design and Application of Squeeze Film Dampers in Rotating Machinery," 25th Turbomachinery Symposium, College Station, TX, Sept. 17-19, pp. 169-188, https://doi.org/10.21423/R1694R.

[7] Della Pietra, L., and Adiletta, G., 2002,"The Squeeze Film Damper over Four Decades of Investigations. Part I: Characteristics and Operating Features," The Shock and Vibration Digest, **34**(1), pp. 3-26.

[8] Della Pietra, L., and Adiletta, G., 2002,"The Squeeze Film Damper over Four Decades of Investigations. Part II: Rotordynamic Analyses with Rigid and Flexible Rotors," The Shock and Vibration Digest, **34**(2), pp. 97-126.3

[9] Parker O-ring Handbook ORD 5700, Parker Hannifin Corporation, Lexington, KY, USA, Accessed April 30th, 2020, https://www.parker.com/Literature/O-Ring%20Division%20Literature/ORD%205700.pdf

[10] San Andrés, L. 1985, "Effects of Fluid Inertia on Squeeze Film Damper Force Response," Ph.D. dissertation, Texas A&M University, College Station, TX.

[11] Vance, J., and Kirton, A., 1974, "Preliminary Investigation of the Dynamic Force Response Coefficients for Squeeze Film Bearing Dampers," Research Report to the US Army Research Office – Durham, AD/A-004 020, University of Florida, Gainesville.

[12] Feder, E., Bansal, P. N., and Blanco, A., 1978, “Investigation of Squeeze Film Damper Forces produced by Circular Centered Orbits,” ASME J. Eng. Gas Turb. Power, **100**(1), pp. 15-21, https://doi.org/10.1115/1.3446313

[13] Zeidan, F., and Vance, J. M., 1989, "Cavitation Leading to a Two Phase Fluid in a Squeeze Film Damper," STLE Tribol. Trans., **32**(1), pp. 100-104, https://doi.org/10.1080/10402008908981868.

[14]Zeidan, F., and Vance, J., 1990, “Cavitation Regimes in Squeeze Film Dampers and their Effect on the Pressure Distribution,” STLE Tribol. Trans., **33(**3), pp. 447-453 https://doi.org/10.1080/10402008908981868

[15] Kuzdzal, M. J., and Hustak, J. F., 1996, “Squeeze Film Damper Bearing Experimental Vs Analytical Results for Various Damper Configurations,” Proceedings of the 25th Turbomachinery Symposium, College Station, Tx, Sept. 17-19, pp. 57-70, https://doi.org/10.21423/R1V36B .

[16] Arauz, G. L., and San Andrés, L., 1996, “Experimental Study on the Effect of a Circumferential Feeding Groove on the Dynamic Force Response of a Sealed Squeeze Film Damper,” ASME J. Tribol., **118**(4), pp. 900-905, https://doi.org/10.1115/1.2831626

[17] Jung, S. Y., San Andrés, L. and Vance, J. M., 1991 “Measurements of Pressure Distribution and Force Coefficients in Squeeze Film Damper - Part I: Fully Open Ended Configuration,” STLE Tribol. Trans., **34**(3), pp. 375-382, https://doi.org/10.1080/10402009108982047

[18] Jung, S. Y., San Andrés, L. and Vance, J. M., 1993 “Measurements of Pressure Distribution and Force Coefficients in Squeeze Film Damper - Part II: Experimental Comparisons,” STLE Tribol Trans., **36**(4), pp. 700-706, https://doi.org/10.1080/10402009108982048

[19] San Andrés, L., Jeung, S.-H., Den, S., and Savela, G., 2016, “Squeeze Film Dampers: An Experimental Appraisal of Their Dynamic Performance,” Proceedings of the 2016 Asia Turbomachinery & Pump Symposium, Marina Bay Sands, Singapore, Feb. 22–25, pp. 1–23.

[20] Jeung, S.-H., 2017, “Experimental Performance of an Open Ends Squeeze Film Damper and a Sealed Ends Squeeze Film Damper,” Ph.D. Dissertation, Texas A&M University, College Station, TX, USA.

[21] San Andrés, L., and Diaz, S., 2002, “Pressure Measurements and Flow Visualization in a Squeeze Film Damper Operating with a Bubbly Mixture,” ASME J. Tribol., **124**(2), pp. 346–350, https://doi.org/10.1115/1.1402133.

[22] San Andrés, L., and Koo, B., 2018, “Effect of Lubricant Supply Pressure on SFD Performance: Ends Sealed With O-Rings and Piston Rings,” Proceedings of the IFToMM Conference on Rotor Dynamics, Río de Janeiro, Brazil, Sept. 23-27, Paper No. IFTOMM2018-0181, https://doi.org/10.1007/978-3-319-99262-4_26 .

[23] San Andrés, L., Koo, B., and Jeung, S.-H., 2019 “Experimental Force Coefficients for Two Sealed Ends Squeeze Film Dampers (Piston Rings and O-Rings), An Assessment of Their Similarities and Differences.” ASME J. Eng. Gas Turb. Power, **141**(2)**,** p. 021024, https://doi.org/10.1115/GT2018-76224

[24] San Andrés, L., and Koo, B., 2020, “Model and Experimental Verification of the Dynamic Forced Performance of a Tightly Sealed Squeeze Film Damper Supplied With a Bubbly Mixture,” ASME J. Eng. Gas Turb. Power, **142**(1), p. 011023, https://doi.org/10.1115/GT2019-90330 .

[25] San Andrés, L., 2009, *Modern Lubrication Theory*, “Experimental Identification of Bearing Force Coefficients,” Notes 14, Texas A&M University Digital Libraries, [Mar 30, 2020], http://oaktrust.library.tamu.edu/handle/1969.1/93254

[26] Fritzen, C. P., 1986, “Identification of Mass, Damping and Stiffness Matrices of Mechanical Systems,”ASME J. Vib. Acoust., **108**(1), pp. 9-16, https://doi.org/10.1115/1.3269310 .

[27] Smalley, A., Darlow, M., and Mehta, R., 1978, “The Dynamic Characteristics of O-Rings,” ASME J. Mech. Design, **100**(1), pp. 132–138, https://doi.org/10.1115/1.3453877 .

Appendix A. Measurement of journal radial clearance

This section shows the process to calculate the radial clearance of the test damper. The SFD radial clearance is:

$$c = \tfrac{1}{2}(D_{BC,ID} - D_{J,OD}) \tag{A.1}$$

where $D_{BC,ID}$ is the bearing cartridge inner diameter and $D_{J,OD}$ is the journal outer diameter. A dial bore gauge determines, with an uncertainty of 1.27 µm (0.05 mil) the BC inner diameter (ID). Figure A1 shows the schematic and cross section view of the bearing cartridge with its dimensions. The bearing cartridge hosts the load cells, accelerometers, and pressure sensors used to conduct the experiments. The annular gap between interior surface of the bearing cartridge and the journal outer surface of the journal locates the lubricant with uniform axial thickness.

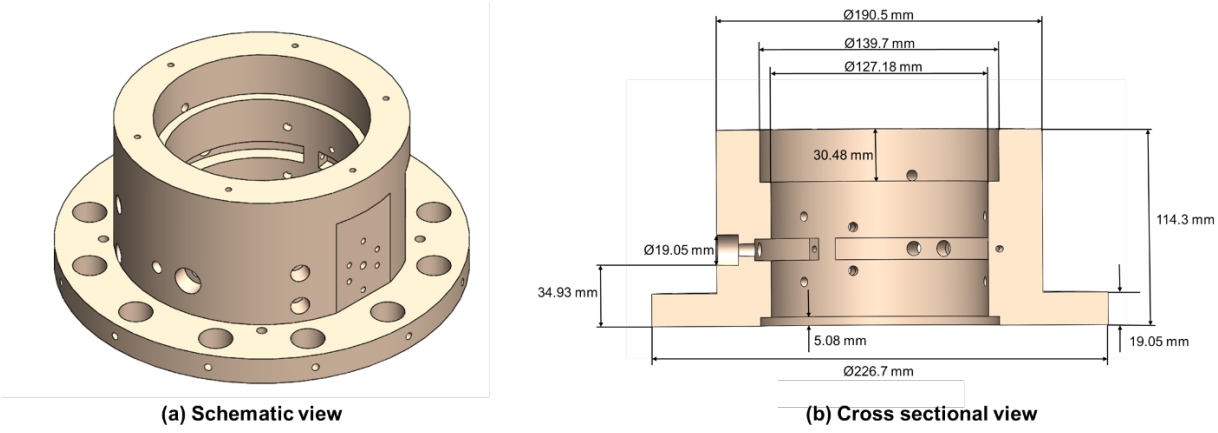

Figure A1. Bearing cartridge (a) schematic view, and (b) cross sectional view.

One set of nine measurements along three different axial planes and three radial planes in the BC surface determine the average $D_{BC,ID}$. Figure A2 displays the $D_{BC,ID}$ measurement planes and angles.

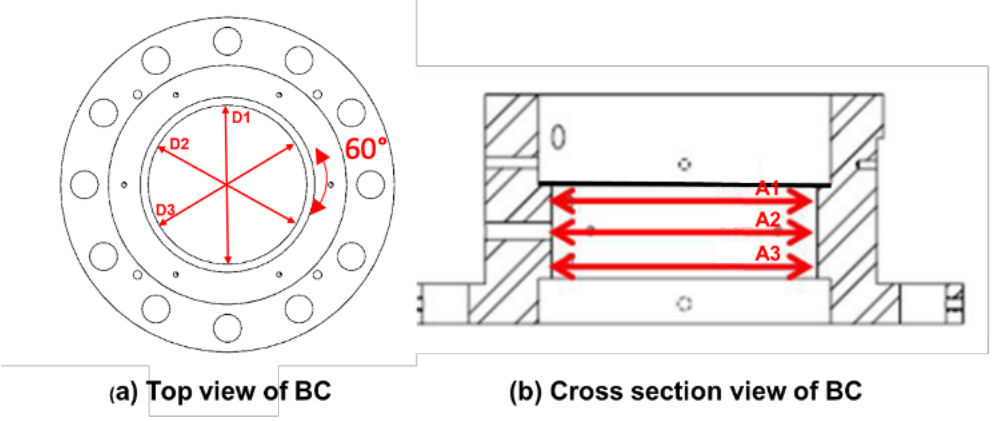

Fig. A2. Bearing cartridge (a) top view, and (b) cross sectional view.

Similarly, measurements of the journal outer diameter (OD) in the top, middle, and bottom plane at three different angles determine the average $D_{J,OD}$. Figure A3 displays the journal measurement locations. An OD micrometer, with an uncertainty of ±1.78 μm (± 0.07 mil), determines $D_{J,OD}$. Table A1 lists measurements of $D_{BC,ID}$ and $D_{J,OD}$.

Table A2 lists the average $D_{BC,OD}$, $D_{J,OD}$ for each measurement plane measurement, and c. From measurements in nine different locations, the total average radial clearance c, is 0.279 mm.

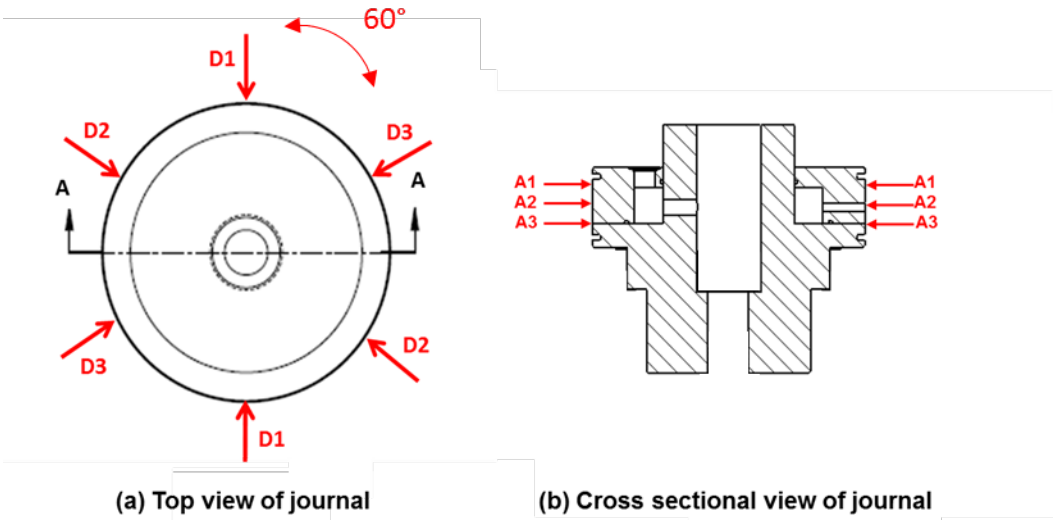

Fig. A3. Journal (a) top view, and (b) cross sectional view.

Table A1. Measurements of $D_{BC,OD}$ and $D_{J,OD}$

Measurement angle	Measurement plane	Diameter [mm (in)]	Diameter [mm (in)]
D1	A1	127.19 (5.0074)	126.62 (4.9852)
	A2	127.20 (5.0077)	126.64 (4.986)
	A3	127.17 (5.0065)	126.62 (4.985)
D2	A1	127.17 (5.0067)	126.62 (4.985)
	A2	127.20(5.008)	126.64 (4.986)
	A3	127.18 (5.007)	126.62 (4.985)
D3	A1	127.19 (5.0075)	126.62 (4.985)
	A2	127.20 (5.0078)	126.64 (4.986)
	A3	127.19 (5.0075)	126.62 (4.985)

Table A2. Average clearance measurement at three axial planes

Plane	Average $D_{BC,OD}$ [mm (in)]	Average $D_{J,OD}$ [mm (in)]	c [mm (in)]
A1	127.18 (5.0072)	126.62 (4.985)	0.282 (0.0111)
A2	127.20 (5.0078)	126.64 (4.986)	0.277 (0.0109)
A3	127.18 (5.007)	126.62 (4.985)	0.279 (0.0110)
Total Average	127.19 ± 0.005 (5.007 ± 0.0002)	126.64± 0.004 (4.985± 0.0002)	0.279 ± 0.006 (0.0110 ± 0.0002)

Appendix B. Measurements of Lubricant Viscosity

The viscosity of the oil used in the SFD test rig must be determined to compare and assess possible changes in viscosity due to temperature change. The BROOKFIELD DVI Viscometer is used to measure the viscosity of the oil vs. temperature. The viscometer consists of a spindle, a small volume cup that acts as a reservoir for the oil, and a water bath device for oil temperature control. With known values of rotational speed, torque, and temperature, the viscometer displays the values of viscosity in cP (centi Poise) for a given temperature. Mobil Velocite™ Oil Numbered Series No. 3 (ISO VG 2) is the test oil in the SFD test rig. Table B1 displays ideal properties of the test lubricant

Table B1. Mobil Velocite ™ No. 3 (ISO VG 2) Manufacturer specification [A2]

Mobil Velocite Oil Numbered Series No. 3 (ISO VG 2)	
cSt @ 40 ºC	2.1
cSt @ 100 ºC	0.95
Pour Point ºC	-36
Flash Point ºC	84
Density @ 15 ºC, kg/L	0.802

A water bath device is used to heat the oil sample in increments of 4 ºC from 25 ºC to 60 ºC., while the viscometer reads viscosity values at 30rpm, such that the measurements fit a decaying exponential function, as noted in Ref. [B1].

The following procedure shows the method to obtain a viscosity measurement.:

- Place 0.5 ml of oil in the cup.
- Heat the water bath to the desired temperature.
- Wait three minutes for thermal equilibrium.
- Turn the spindle for one minute.
- Read and record the viscosity measurement.
- Continue in increments of 4 ºC until the maximum temperature is achieved (60º).

Figure B1 shows measurements from prior years, along with current measurements and curve fits derived from the measurements and from the manufacturer specifications. Three

measurement sets, performed in July 2019, represent the updated estimation of the lubricant viscosity as a function of temperature.

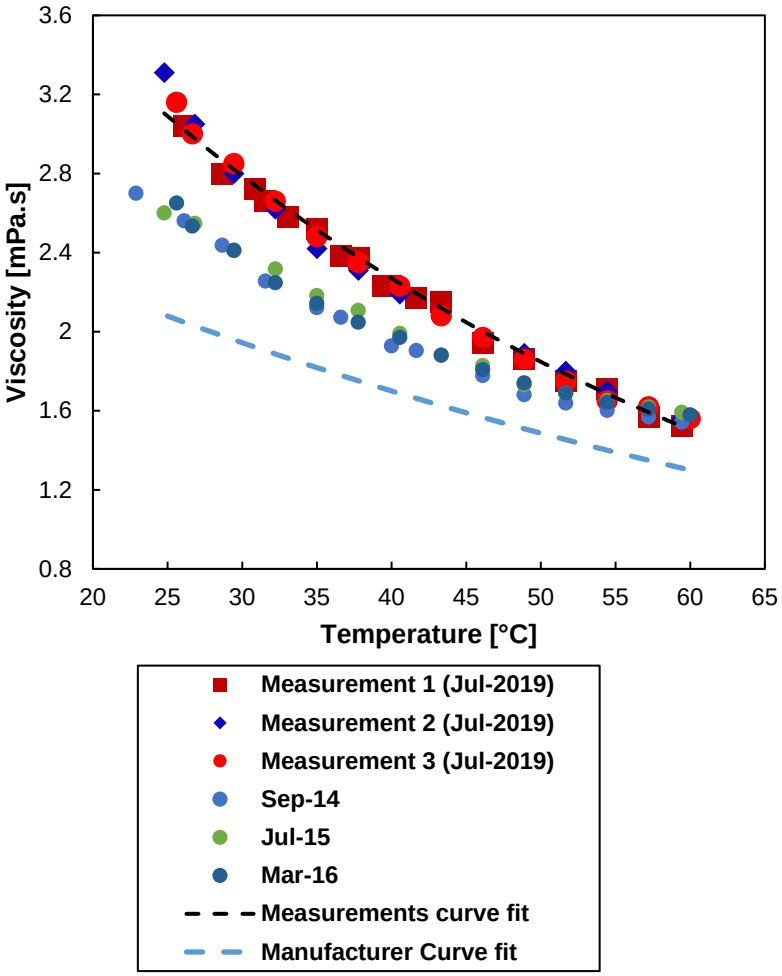

Figure B1. Oil viscosity measurements.

The current measurements indicate a dynamic viscosity of 2.2 mPa-s at 40 ºC. The manufacturer specifies a dynamic viscosity of 1.68 mPa-s at 40 ºC. Prior measurements from 2014 to 2016 show an oil viscosity increment of ~15% compared to the specifications, and ~25% compared to the most recent set of measurements. The difference between the manufactured viscosity magnitudes and the measured magnitudes is likely due to the mix of multiple oil batches in the experimental facility oil reservoir over the span of multiple years testing. Different batches of the same type of oil may have different viscosity magnitudes, in addition to particulate gathering from older batches could further alter the oil viscosity. The changes in viscosity over time are expected, considering the accuracy of the viscometer (± 0.1 mPa-s) and the steady increment in

viscosity compared to measured values from 2014 to 2016. Measurements of the weight in a known volume of a small sample of oil determines its density at room temperature of 20 ºC. The oil density $\rho =$ 0.780 kg/L, is different from the manufacturer specification (see Table B1) by only ~3%. This minuscule difference discards air entrainment in the lubricant, another cause of viscosity increment.

Roelands et al. [B1] establish a standard relationship between oil viscosity and temperature:

$$\mu = \mu_R e^{-a_v (T - T_R)} \tag{B.1}$$

where μ is the predicted viscosity at temperature T in ºC. The viscosity at room temperature (T_R = 20 ºC) is μ_R = 3.40 mPa-s , obtained from the 2019 measurements. The oil temperature to viscosity coefficient, a_v, is:

$$a_v = \frac{-ln \frac{\mu_2}{\mu_R}}{T_2 - T_R} = 0.02 \frac{1}{^{o}\text{C}} \tag{B.2}$$

where μ_2 = 1.54 mPa-s and T_2 = 60ºC are the last values of viscosity and temperature, respectively.

References

[B1]Roelands, C.J.A, Vlugter, J.C., and Waterman, H.I., 1963, "The Viscosity-Temperature-Pressure Relationship of Lubricating Oils and its Correlation With Chemical Constitution" J. Basic Eng., **85**(4), pp. 601-607.

[B2] "Mobil Velocite™ No 3 (ISO VG 2) Manufacturer specification sheet,", Hydraulic oils Typical Properties, Mobil, Accessed February 2020. https://www.mobil.ca/en-CA/lubricants/industrial/lubricants/products/products/mobil-velocite-oil-no-3

[B3] Ng, W.S., Levesley, M. C., and Priest, M., 2005, "Effects of Bubble son the Viscosity Properties of Lubricants," ASME Paper No. WTC2005-64114.

Appendix C. Flow Measurements in Sealed Ends SFD

Figure C1 displays measurements of the lubricant flow rate vs. supply pressure into the ORs sealed journal and open to ambient journal. The oil enters through a feedhole in the journal located at θ = 45° and at the midplane of the journal (z = 0). Two different flow meters record P_s vs Q_s. The first one records the inlet flow rate from 0.05 to ~2 LPM. With an accuracy of ±3% within the full measuring range (0.05-4) LPM [C1]. The second flow meter, measuring in GPM, has an accuracy of ±5% over the full measuring scale (3.78-41.65 LPM), and a maximum resolution of 0.04 LPM [C2]. Note the gauge supply pressure, and during the test, the ORs sealed journal shows no leakage through the O-ring seals. The same measurement is performed without any seals in the ends of the journal. The measurements show that for the same supply pressure, the open ends journal has a flow rate 2.70 times higher than the ORs sealed.

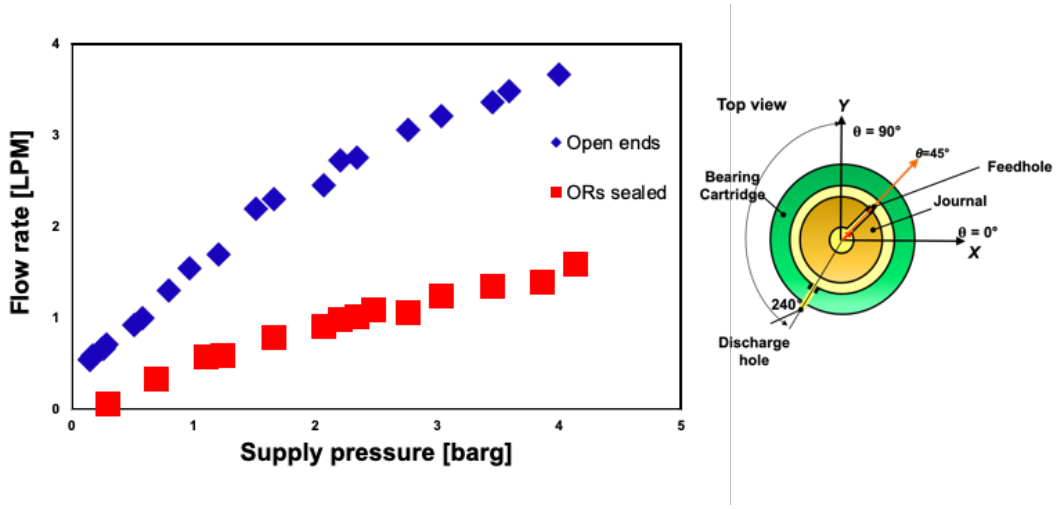

Figure C1. Lubricant flowrate (Q_S) vs. inlet supply pressure (P_S) for ORs sealed journal and open ends journal. Lubricant inlet a feedhole (θ = 45° at mid-plane, z = 0) and lubricant discharges through hole (θ = 240° and z =1/4L).

References

[C1] "PTFE Liquid Flow Sensor Manufacturer Specification Sheet," FPR1501 Series Flow Sensor, Omega, Accessed April 27th, 2020, https://www.omega.co.uk/pptst/FPR1500.html

[C2] "GPI Turbine Flowmeters Manufacturer Specification Sheet," A1 Series Commercial Grade Meter, GPIMETERS, Accessed April 2nd , 2020, https://www.gpimeters.com/prodview.asp?pagename=/A109GMA025NA1

Appendix D. Identification of Physical Parameters for Dry Test System

Circular centered orbit tests (static eccentricity $e_s = 0$) with a dry system (no lubricant supplied) serve to estimate the test system structural parameters. These parameters are the structure stiffness (K_{st}), system remnant mass (M_{st}) and structure damping (C_{st})**.** Prior to the tests, a scale measures the BC from disassembling the testing apparatus, such that $M_{BC} = 15.2 \pm 0.05$ kg. Two orthogonally positioned electromagnetic shakers deliver single frequency loads, 90° out of phase, over a frequency range from 30 to 120 Hz. Multiple tests with clockwise ($+\omega$) and counter clockwise ($-\omega$) frequencies produce data to determine the complex dynamic stiffness of the dry system. The amplitude of the circular motions is r/c=0.05.

Figure D1 presents the measured real and imaginary parts of the complex dynamic stiffness (**H)** and the physical model curve fits for the dry system versus frequency. The graphs include results for tests conducted without ORs installed ($\mathbf{H}_{st}$), and with OR seals in place ($\mathbf{H}_{st+OR}$). Note that as $\omega \to 0$, Im($\mathbf{H}_{st+OR}$) does not have a null magnitude, showing a quadrature stiffness ($K_{0,OR}$). This demonstrates the dissipative forces in the elastomeric seals, that quantify their identified equivalent viscous damping. However, Im($\mathbf{H}_{st}$) shows that $K_{0,st}$, is nil.

Table 2 lists the dry system without ORs identified force coefficients, the dry system natural frequency and damping ratio, with the bearing cartridge mass, valid over a frequency range f = 30-120 Hz. Similarly, Table 3 displays the dry system identified force coefficients with ORs installed. Table 4 shows the OR identified force coefficients. Note that the shown force coefficients, are representative of the selected frequency range.

Measurements of the real part of the complex stiffness Re($\mathbf{H}_{st+OR}$) show the elastomeric seals do increase the system stiffness considerably, up to ~45 %, compared to Re($\mathbf{H}_{st}$) This causes an increment in the system natural frequency by ~ 25%. Addition of the ORs to the dry structure significantly increases the damping ratio by 3 times in the X axis, and two times in the Y axis.

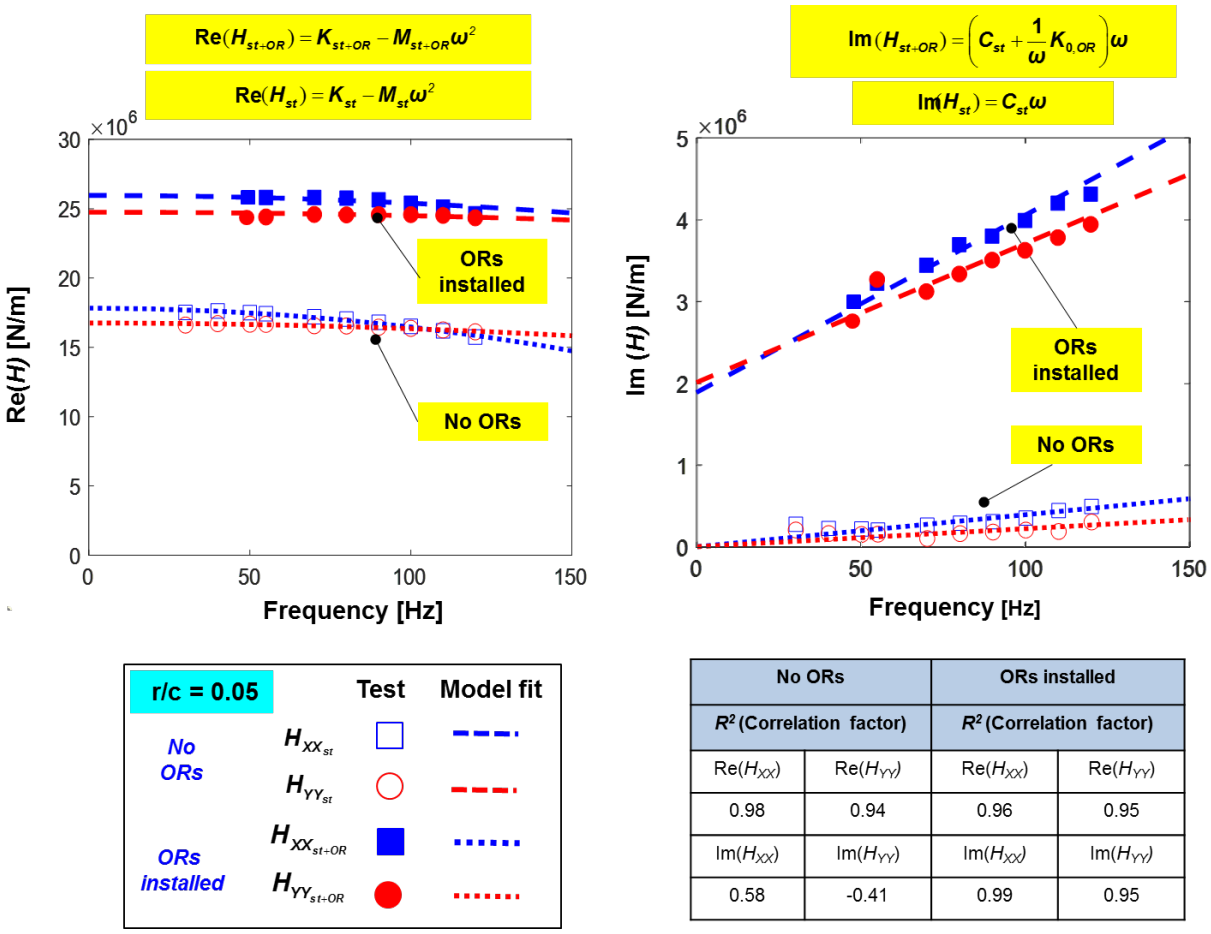

No ORs		ORs installed	
R^2 (Correlation factor)		R^2 (Correlation factor)	
Re(H_{XX})	Re(H_{YY})	Re(H_{XX})	Re(H_{YY})
0.98	0.94	0.96	0.95
Im(H_{XX})	Im(H_{YY})	Im(H_{XX})	Im(H_{YY})
0.58	-0.41	0.99	0.95

Fig. D1. Dry test system (without lubricant). Real and imaginary parts of system direct complex dynamic stiffness versus excitation frequency. Centered circular orbit dynamic load tests. Orbits with radius *r/c* = 0.05 and static eccentricity e_s/c = 0.0. Frequency range from 30 Hz to 120 Hz.

The inset table in Fig.D1 shows the correlation factor in Re($\mathbf{H}_{st}$) and Re($\mathbf{H}_{st+OR}$), is high ($R^2 >$ 0.9), indicating that the model represents the stiffness of the structure and ORs. However, the correlation factor in Im($\mathbf{H}_{st}$) is low ($R^2 << 1$), indicating the structural damping ($\mathbf{C}_{st}$) is not of viscous type, as expected. Incidentally, the identified damping with quadrature stiffness ($\mathbf{C}_{st+OR}$ + $\mathbf{K}_{0,OR}$) shows good correlation (R^2 > 0.9) to the model. Albeit, the viscoelastic and structural damping $C_{st+OR}/C^* \sim$ 0.08 remains a small portion of the analytical viscous damping in the SFD

The experimental results show that the system is slightly orthotropic ($K_{XX} > K_{YY}$, $C_{XX} > C_{YY}$, $M_{XX} > M_{YY}$) since the experimental apparatus includes several inlet and outlet lubricant lines and connections to the various sensors. The experimentally derived force coefficients (K, C, M) have a total uncertainty of U_K = 4.3%, U_C = 6.3%, U_M = 12.6%, that establish confidence intervals in the estimated force coefficients.

Appendix E. Uncertainty in identified Force Coefficients[2]

This section presents the calculation of the uncertainty in the identified SFD force coefficients. The total uncertainty of the estimated force coefficients is comprised of bias uncertainty, precision uncertainty (curve fit) and measurement variability. $U_{B,}$ and U_P denote the bias and precision uncertainties, respectively.

Bias uncertainty (U_B)

Bias uncertainty in sensors and transducers is defined as the systematic difference between the reference measurement and the recorded value [E1]. Although proper calibration and obtaining measurements within the linear range of the sensor remove large known biases, there is an error associated with the sensors and DAQS resolution.

The DAQs consists of a NI cDAQ-9172 board with eight NI 9215 analog input boards that record the output voltage from the sensors. The product specification sheet [E2] states that over the maximum admissible voltage of ± 10.4 V, the NI 9215 board has a percent of reading uncertainty (gain error) equal to $U_{B,gain} = 1.1\%$, and a percent of range uncertainty (offset error) $U_{B,offset} = 0.8\%$. The NI cDAQ-9172 board has an analog to digital converter (ADC) with a resolution of 16 bits [E3], with the input voltage of ± 10.4 V. Thus, the highest voltage resolution in the DAQs over the voltage range corresponds to 0.31 mV. The bias uncertainty in the DAQs over a maximum input voltage of ± 10.4 V is:

$$U_{B,DAQ} = \sqrt{U^2_{B,offset} + U^2_{B,gain}} = 1.3\% \qquad \text{(E.1)}$$

The eddy current sensors used to measure the BC relative displacements to the journal have a sensitivity of 40 mV/μm. Within the highest DAQ resolution of 0.31 mV, the eddy current sensors have an uncertainty of 7.75 μm. The mean absolute recorded displacement at the nominal whirling motion for measurements recorded in the nominal condition r/c = 0.15 and P_S = 0.7 bar(g) from ω = 10 – 70 Hz, is 10.50 μm, thus the displacement uncertainty is $U_{B,D}$ = 0.1%.

The piezoelectric accelerometers have a sensitivity of 10.93 mV/(m/s^2), along with the DAQ resolution of 0.31 mV, gives an uncertainty of 0.03 m/s^2 [E4]. For the mean absolute recorded

[2]This section follows portions of the uncertainty analysis presented in [20]

acceleration of 3.22. m/s^2 in the nominal condition r/c = 0.15 and P_S = 0.7 bar(g) from ω = 10 – 70 Hz, the uncertainty in the measured acceleration is $U_{B,A}$ = 0.9 %.

The load cells have a sensitivity of 2.25 V/N and an uncertainty of ± 0.14 N due to the voltage resolution in the DAQS. For the mean absolute recorded dynamic load of 22.83 N in the nominal operating conditions, the uncertainty in the load measurement is $U_{B,L}$ = 0.8% .

The individual measurement uncertainties comprise the bias uncertainty in the dynamic complex stiffness from measurements in the average condition:

$$U_{B_{SFD}} = \sqrt{U_{B,DAQ}{}^2 + U^2{}_{B,D} + U^2{}_{B,L}} = 1.2\% \tag{E.2}$$

Subtraction of the force coefficients of lubricated system force coefficients with ORs installed, from the force coefficients of the dry system with ORs installed and the force coefficients of the dry structure force coefficients determines the SFD force coefficients. Thus:

$$(K,C,M)_{SFD} = (K,C,M)_L\text{-}(K,C,M)_{st}\text{-}(K,C,M)_{OR} \tag{E.3}$$

Therefore, the propagation of the bias uncertainty in the estimated force coefficients is:

$$U_{B_{SFD}} = \sqrt{U_{B_L}{}^2 + U^2{}_{B_{OR}} + U^2{}_{B_{st}}} = 2.1\% \tag{E.4}$$

Precision uncertainty (U_P)

Precision uncertainty is related to the estimation of the force coefficients in the physical model curve fit. Circular excitations over a range of selected frequencies estimate the complex dynamic stiffness of the system to identify their force coefficients. Curve fits of the physical model Re(**H**) = (**K**–**M** ω^2), Im(**H**) = (**C** ω^2) estimate the force coefficients. The coefficient of determination (R^2) defines the goodness of fit between the physical model and the measurements for both curve fits [E5] in the real and imaginary parts of **H**. R^2 is also defined as the ratio of the sum of squared regression *SSR*, divided over the total variation, *SST*:

$$R^2 = \frac{SSR}{SST} = \frac{\sum_{i=1}^{N}(y_i - f_i)^2}{\sum_{i=1}^{N}(y_i - \bar{y}_i)^2} \tag{E.5}$$

Where y_i denotes each measurement value of Re(**H**) and Im(**H**), from 1 to N frequency measurements, while $\bar{y}$ is the mean of the y_i measurements. Then, f_i is the physical model value

corresponding in Re(**H**) and Im(**H**)to each y_i measurement. Coleman [E6] presents the confidence bounds for the coefficients estimated by the curve fit of the physical model:

$$\psi_{fit} = \pm t_d \sqrt{S} \tag{E.6}$$

Where t_d is the inverse Student's t cumulative distribution function, given a 95% confidence level. S is a vector of the diagonal elements from the estimated covariance matrix of the coefficient estimates, $(\mathbf{A}^T\mathbf{A})^{-1}SSR^2$. Where the matrix **A** represents the Jacobian of the measured values in Im($\mathbf{H}_{XX}$, $\mathbf{H}_{YY}$) and Re($\mathbf{H}_{XX}$, $\mathbf{H}_{YY}$) with respect to the curve fits of the physical model, Re(**H**) = $(\mathbf{K}-\mathbf{M}\,\omega^2)$ Im(**H**) = $(\mathbf{C}\,\omega^2)$ The matrix $\mathbf{A}^T$ is the transpose of **A,** and *SSR* is the sum of squared regression, as noted in Eq. E.5. For a nominal condition of r/c = 0.15 and P_S = 0.7 bar(g), the average of the direct force coefficients is K=22.22 MN/m, C = 31.12 kN-s/m, and M=61.95 kg. From Eq. E.6, the precision uncertainty due to the curve fit in the physical model in the estimated force coefficients is:

$$U_{P_K} = \frac{\psi_{fit,K}}{K} = 2.8\% \tag{E.7}$$

$$U_{P_C} = \frac{\psi_{fit,C}}{C} = 4.3\% \tag{E.8}$$

$$U_{P_M} = \frac{\psi_{fit,M}}{M} = 6.0\% \tag{E.9}$$

Uncertainty due to variability (U_V)

The uncertainty due to variability is related with the repeatability of measurements. To address the repeatability in the experiments and in the estimated force coefficients, multiple test sets include three sets of measurements in the same operating conditions. A total of nine tests (three in each r/c = 0.1, r/c = 0.15 and r/c = 0.2) comprise the experimental results for a lubricated system. The tests sets have a standard deviation that demonstrates the variability in the measurements. The confidence intervals due to variability [E2] are:

$$\psi_V = t_V S_V \tag{E.10}$$

Where t_V = 2.45 denotes the t Student's value for a 95% confidence interval, and S_V is the standard deviation in the N=3 test sets:

$$S_x = \sqrt{\frac{1}{(N-1)}\sum_{i=1}^{N}(x_i - \bar{x})^2} \tag{E.11}$$

Where x represents the estimated force coefficients, $\bar{x}$, the average of all the measured data and i is the index number. Table E1 shows the lubricated system identified force coefficients for ORs sealed SFD operating at the nominal condition r/c = 0.15 and P_S= 0.7 bar(g), over a frequency range ω = 10 -70 Hz.

Table E1. Identified system force coefficients(K,C,M)$_L$ for ORs sealed SFD. Supply pressure P_S = 0.7 bar(g), r/c = 0.15 and frequency range from 10 Hz to 70 Hz.

Test #	K_{XX} [MN/m]	K_{YY} [MN/m]	C_{XX} [kN-s/m]	C_{YY} [kN-s/m]	M_{XX} [kg]	M_{YY} [kg]
1	23.84	21.56	33.10	28.03	63.21	53.75
2	23.20	21.29	33.41	28.94	66.72	57.63
3	23.2	21.56	33.7	29.46	68.46	59.21

Substitution of Eqs. E.11 in E.10 divided over the average estimated force coefficients gives the uncertainty due to variability in the identified force coefficients:

$$U_{V_K} = \frac{\psi_K}{K} = 2.6\% \tag{E.12}$$

$$U_{V,C} = \frac{\psi_C}{C} = 4.2\% \tag{E.13}$$

$$U_{V,M} = \frac{\psi_M}{M} = 10.9\,\% \tag{E.14}$$

Total uncertainty

The propagation of the total uncertainty in the identified SFD dynamic forced coefficients is:

$$U_K = \sqrt{U_{P,K}^2 + U_{B,SFD}^2 + U_{V,K}^2} = 4.3\% \tag{E.15}$$

$$U_C = \sqrt{U_{P,C}^2 + U_{B,SFD}^2 + U_{V,C}^2} = 6.3\% \tag{E.16}$$

$$U_M = \sqrt{(U_{P,M}^2 + U^2_{B,\,SFD} + U^2_{V,\,st})} = 12.6\% \qquad \text{(E.17)}$$

References

[E1] San Andrés, L., 2019, *Measurements of Sounds and Vibration*, "Sensor calibration & uncertainty in measurements and engineering analysis," Texas A&M University, https://rotorlab.tamu.edu/me459/NOTES%205%20Sensors%20and%20Uncertainty%20Analysis.pdf [March 23rd, 2020].

[E2] "NI 9215 Datasheet, " Datasheet for NI 9215 analog input module, National Instruments, 2016.

[E3] "NI cDAQ -917x User Manual," User manual for NI compact DAQ 9171/9174/9178 USB Chassis, National Instruments, July, 2011.

[E4] "353B33 PCB™ Product Datasheet" Product specification sheet for 353B33 piezoelectric accelerometer, PCB Piezotronics ™, July, 2007.

[E5] Fornasini, P., 2008, *The Uncertainty in Physical Measurements,* Springer, New York, pp. 184-189.

[E6] Coleman, H. W., and Steele, G. W., 1998, *Experimentation and Uncertainty Analysis for Engineers*, John Wiley & Sons, New York.

[E7] Beckwith, T., Marangoni, R., and Lienhard., J., 1993, "Mechanical Measurements," Prentice Hall. 5th edition, pp. 82.

Appendix F. Lubricated System Cross-coupled Dynamic Stiffnesses

Figure F1 displays the real and imaginary parts of the cross-coupled complex dynamic stiffnesses Re($H_{XY,\ YX}$)$_L$, Im($H_{XY,\ YX}$)$_L$, and physical curve fits (*KCM* model). In the model, Re($\mathbf{H}_L$) $\rightarrow$ ($\mathbf{K}_L - \omega^2\mathbf{M}_L$). and Im($\mathbf{H}_L$) $\rightarrow$ ($\mathbf{C}_L\omega$). The damper operates with a constant supply pressure of 0.7 bar(g) and with whirl orbit radii r/c = 0.1, 0.15 and 0.2. The inset tables list the cross-coupled damping and added mass coefficients, along with R^2 to the *KCM* model. The model curve fits show low correlation factor $R^2 < 1$, with real and imaginary values of H_{XY} and H_{YX} at least one order of magnitude lower than $\mathbf{H}_L$ show values of stiffness, Additionally, the stiffness and damping coefficients approach zero, thus, the cross-coupled coefficients in the lubricated system are negligible for the direct SFD coefficients..

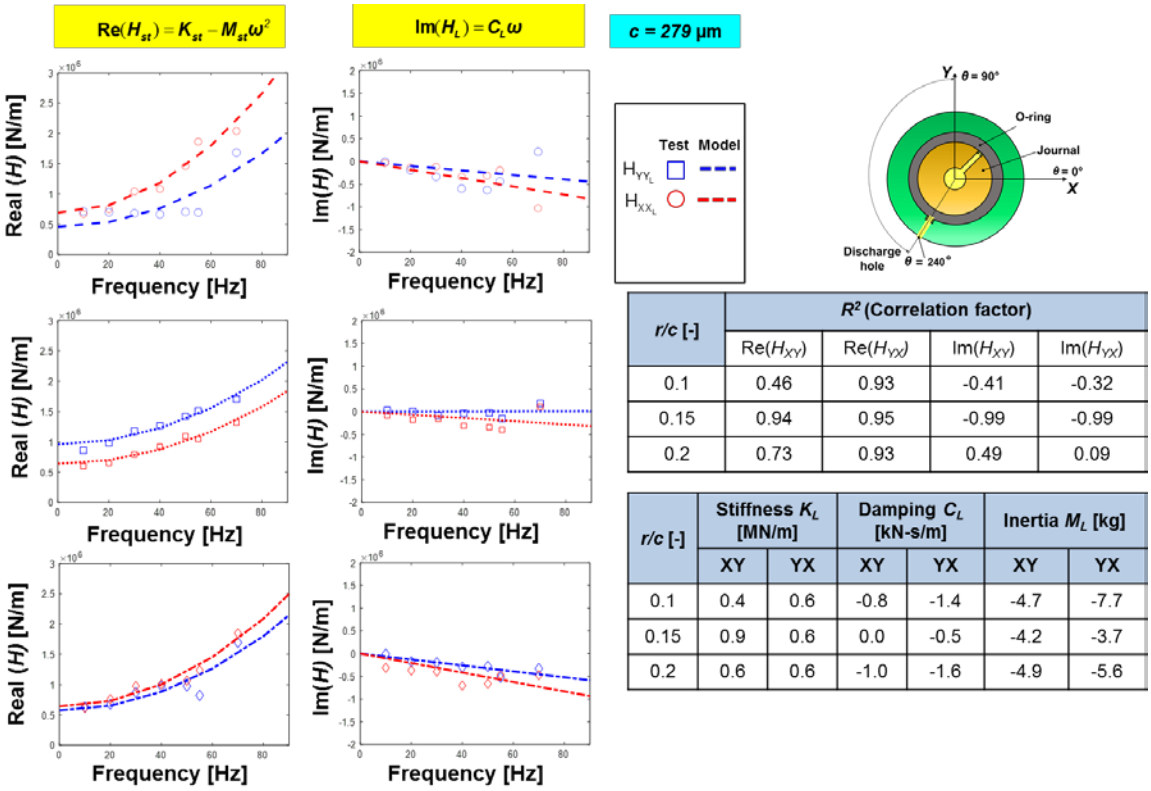

r/c [-]	R^2 (Correlation factor)			
	Re(H_{XY})	Re(H_{YX})	Im(H_{XY})	Im(H_{YX})
0.1	0.46	0.93	-0.41	-0.32
0.15	0.94	0.95	-0.99	-0.99
0.2	0.73	0.93	0.49	0.09

r/c [-]	Stiffness K_L [MN/m]		Damping C_L [kN-s/m]		Inertia M_L [kg]	
	XY	YX	XY	YX	XY	YX
0.1	0.4	0.6	-0.8	-1.4	-4.7	-7.7
0.15	0.9	0.6	0.0	-0.5	-4.2	-3.7
0.2	0.6	0.6	-1.0	-1.6	-4.9	-5.6

Fig. F1. Lubricated OR sealed ends damper (c = 279 µm). Real and imaginary parts of cross-coupled complex dynamic stiffnesses ($H_{XY,\ YX}$)$_L$ vs whirl frequency Parameters identified in the frequency range from 10 to 70 Hz. CCO with radius r/c = 0.1, r/c = 0.15 and r/c = 0.2. P_S = 0.7 bar(g).

Appendix G Measurements of dynamic pressure in the damper film lands[3]

Figure 10 shows the location of the pressure sensors, in the bearing cartridge (BC). Six piezoelectric dynamic pressure sensors (P_1-P_6) installed in the BC around its circumference. Two groups of three transducers ($P_{1\text{-}3}$, $P_{4\text{-}6}$) spaced by 90º, record the film dynamic pressure at the top, bottom and middle (Top, Mid, Btm). Each group ($P_{1\text{-}3}$, $P_{4\text{-}6}$) is spaced by 15º. A piezoelectric pressure sensor (P_7) measures the film dynamic pressure in the oil plenum inside the journal (see Fig. 3(a)). This section shows measured pressure profiles in the film lands, from the CCO, as well as an analysis of the dynamic pressure, as a function of the orbit radius r and whirl frequency ω. Figure G1 shows section views of the BC: (a) top view, (b) axial view and (c) unwrapped view, with the position of the pressure transducers.

This section presents measurements obtained from pressure sensor P_4, located at $\theta = 225^o$, and z=0 for an ORs sealed damper supplied with lubricant at P_S = 0.7 bar(g). Figures G2 to G4 show recorded dynamic pressure profiles for whirl radii r/c = 0.10, 0.15 and 0.20, respectively. The figures display three whirl periods (T= 11ms). The recorded film thickness h, from pressure measurements in the same location is:

$$h_{(\theta,t)} = c + X_{(t)}cos\theta + Y_{(t)}sin\theta \quad \text{(G.1)}$$

$$X_{(t)} = rcos(\omega t + \varphi_X) \quad \text{(G.1a)}$$

$$Y_{(t)} = rcos(\omega t + \varphi_Y) \quad \text{(G.1b)}$$

Where r is the orbit radius, φ_X and φ_Y are the arguments of the fundamental components of the Fourier series-built functions from the measured displacements along the X,Y axes. In Figs. G2-G4, the dotted lines P_{atm} and P_0 mark the atmospheric and absolute zero pressure. In the Figures, all the pressure profiles for squeeze velocities below $r\omega$~21 mm/s show a sinusoidal shape without flat pressure peaks, valleys or distorted profiles, where cavitation or air entrance are present in the film lands. Above this magnitude of squeeze velocity, the dynamic pressure profiles show flat zones near the maximum film thickness region, below P_{atm}, denoting oil vapor cavitation. In the squeeze region where h decreases, at $r\omega$ > 21 mm/s, the dynamic pressure shows sharp spikes, characteristic of bubbles bursting, marked with a red ellipse. In this case, the bubbles bursting could either be from cavitating oil or air in the film lands. Incidentally, various pressure profiles at $r\omega$ > 21 mm/s denote a flat pressure peak, marked with a green ellipse. This is particularly noticeable in Fig. G3, in at ω=90 Hz and Fig. G4 at ω=70 Hz. Thus showing that in regions where

[3] This section reproduces information presented in Ref. [20].

the dynamic pressure should keep increasing, but remains fairly constant, thus evidencing air entrapped in the film lands being compressed by the squeeze film.

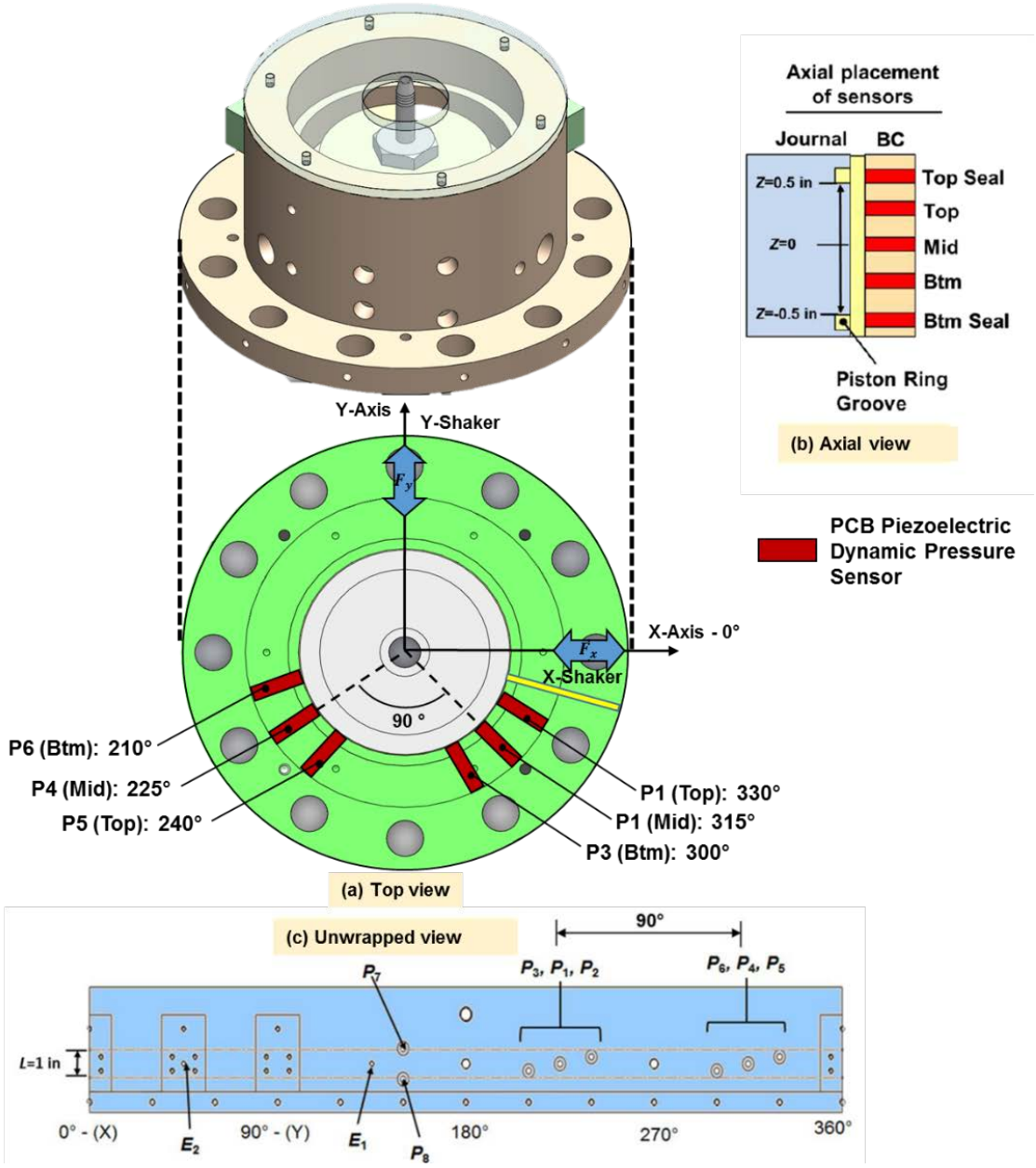

Fig G1. Schematic views of the location of pressure sensors in the BC: (a) top view, (b) axial view and (c) unwrapped view. Schematic views taken from Ref [16].

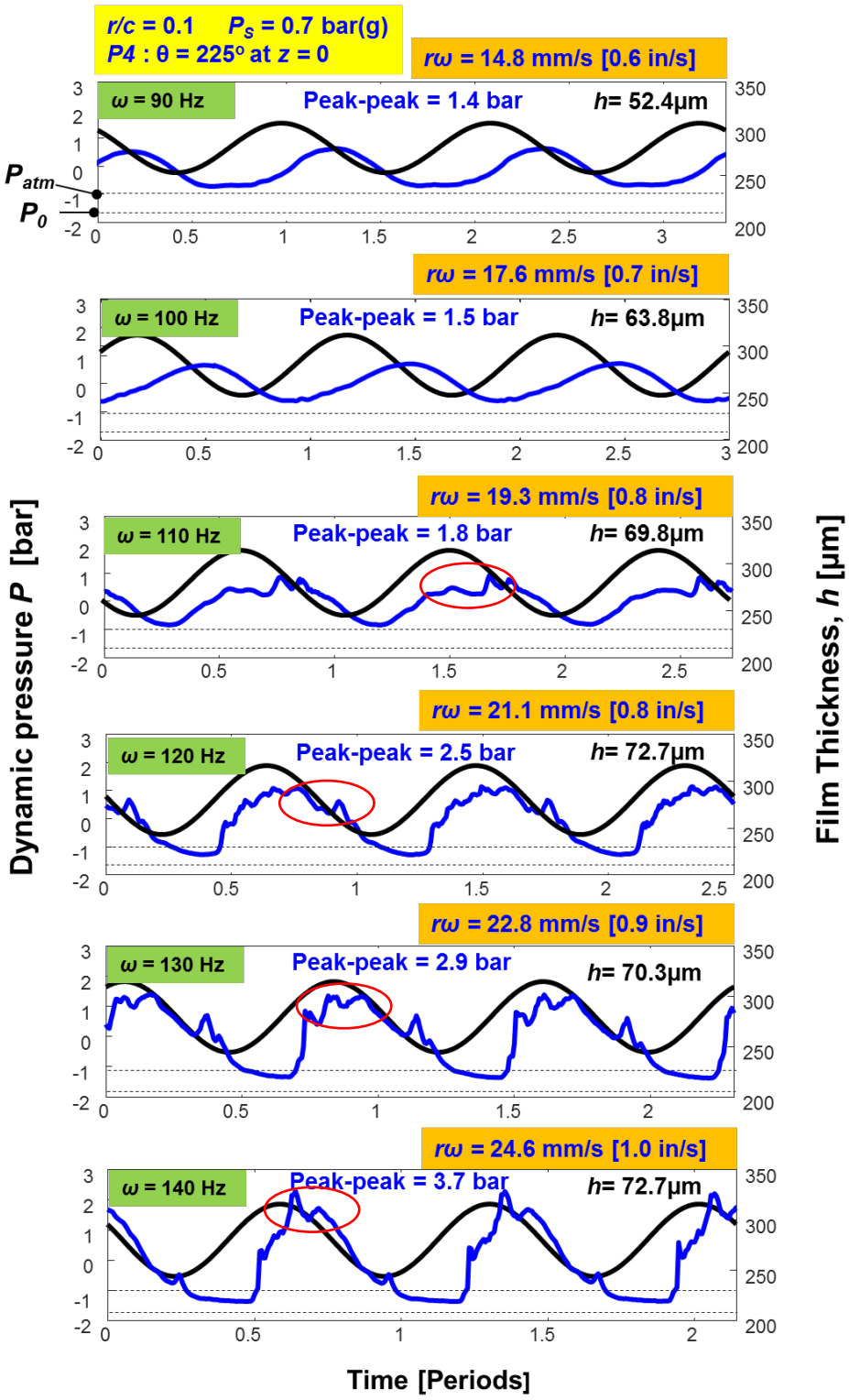

Fig. G2. ORs sealed damper P_S=0.7 bar(g). Dynamic film pressure (*P*) and film thickness (*h*) recorded at θ=225° (*P4*) versus time (*t*/*T*) for measurements at mid-plane (*z* =0). Circular entered orbits with frequency ω = 90 Hz to 140 Hz, with radius *r*/*c* = 0.1

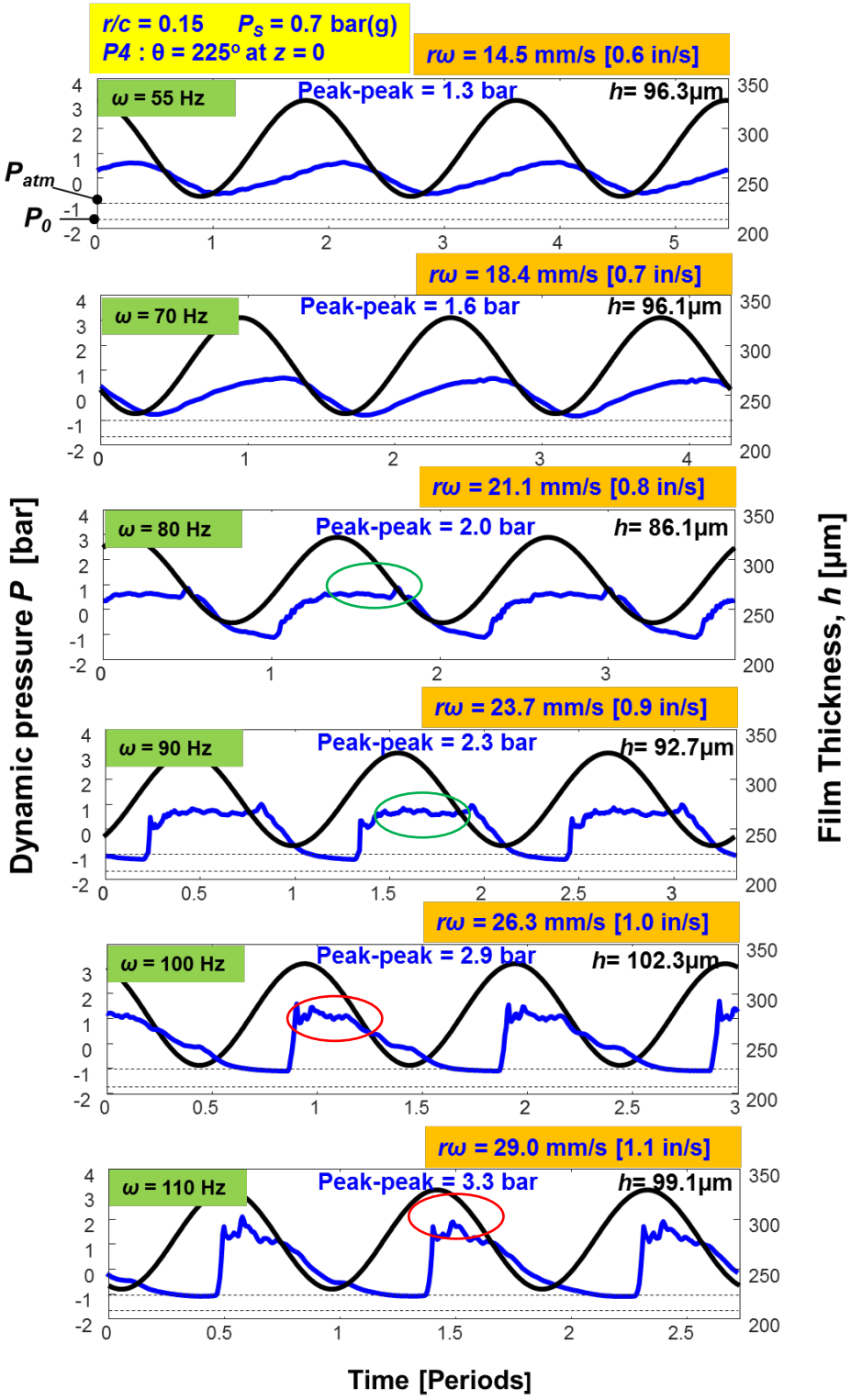

Fig G3. ORs sealed damper P_S=0.7 bar(g). Dynamic film pressure (*P*) and film thickness (*h*) recorded at θ=225° (*P4*) versus time (*t*/*T*) for measurements at mid-plane (*z* =0). Circular entered orbits with frequency ω = 55 Hz to 110 Hz, with radius *r*/*c* = 0.15

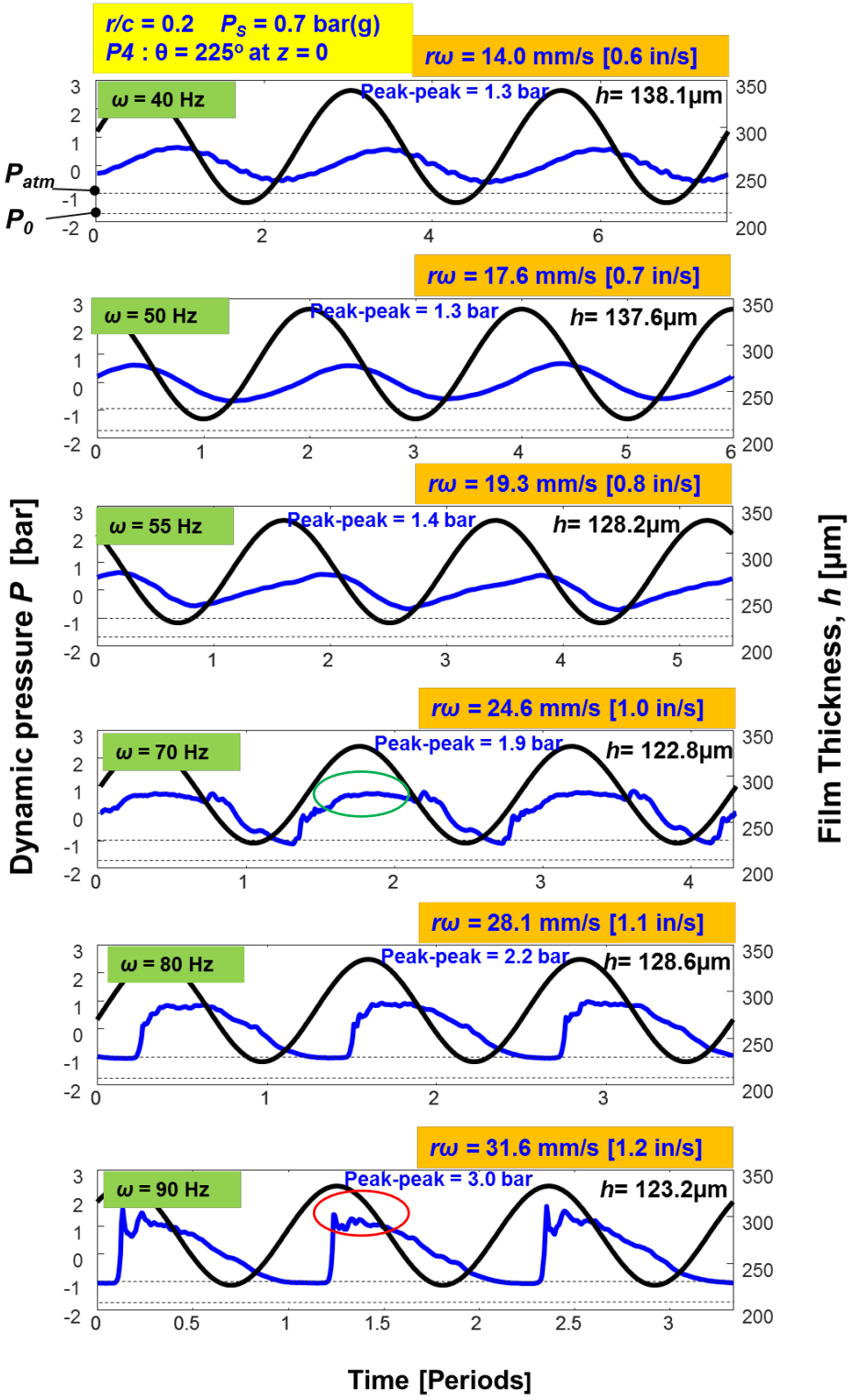

Fig G4. ORs sealed damper P_S=0.7 bar(g). Dynamic film pressure (P) and film thickness (h) recorded at θ=225° ($P4$) versus time (t/T) for measurements at mid-plane (z =0). Circular entered orbits with frequency ω = 40 Hz to 90 Hz, with radius r/c = 0.2

Figure G5 shows the recorded peak-to-peak dynamic pressures, for CCO tests with lubricant pressure P_S = 0.7 barg. The peak-to-peak pressures show a steady increase, with similar magnitude up to 80 Hz. At frequencies above 80 Hz, the pressures show an unclear trend for the orbit radii r/c = 0.15 and 0.10. In the lowest orbit radius, the magnitude of the pressures substantially drops at 90 Hz and increases steadily again up until 140 Hz. For r/c = 0.15, there is a sudden drop in the peak-to-peak pressure magnitudes. In the recorded pressures, either the flat pressure zones with oil vapor cavitation or air entrainment likely disrupt the increasing peak-to-peak pressure amplitude

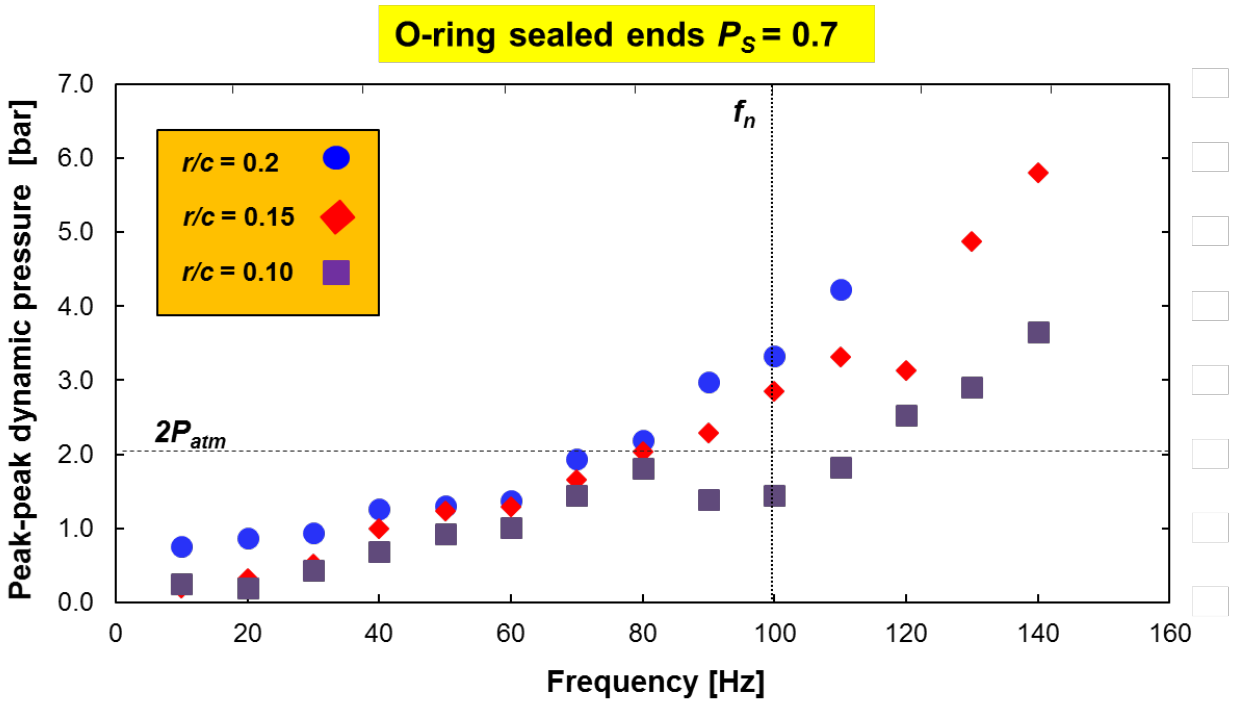

Fig G5. ORs sealed damper P_S=0.7 bar(g). Recorded peak-to-peak dynamic pressures at θ=225°, z=0 (*P4*) versus frequency). Circular entered orbits with frequency ω = 10 Hz to 140 Hz, with radius r/c = 0.10, 0.15 and 0.20